

See discussions, stats, and author profiles for this publication at: <https://www.researchgate.net/publication/49652972>

Molecular Driving Forces for Z/E Isomerization Mediated by Heteroatoms: The Example Hemithioindigo

ARTICLE in THE JOURNAL OF PHYSICAL CHEMISTRY A · DECEMBER 2010

Impact Factor: 2.69 · DOI: 10.1021/jp107899g · Source: PubMed

CITATIONS

18

READS

39

5 AUTHORS, INCLUDING:



Artur Nenov

University of Bologna

26 PUBLICATIONS 172 CITATIONS

[SEE PROFILE](#)

Molecular Driving Forces for Z/E Isomerization Mediated by Heteroatoms: The Example Hemithioindigo

Artur Nenov,[†] Thorben Cordes,^{‡,§} Teja T. Herzog,[‡] Wolfgang Zinth,[‡] and Regina de Vivie-Riedle*,[†]

Department of Chemistry and Biochemistry, Ludwig-Maximilians-Universität München, Butenandtstrasse 11, D-81377 München, Germany, and BioMolecular Optics and Munich Center for Integrated Protein Science CIPSM[‡], Fakultät für Physik, Ludwig-Maximilians-Universität München, Oettingenstrasse 67, D-80538 München, Germany

Received: August 20, 2010; Revised Manuscript Received: November 12, 2010

A combined experimental and theoretical investigation of photoinduced Z/E isomerizations is presented. Unsubstituted Hemithioindigo is selected as a representative minimal model to unravel the reaction mechanism in the presence of heteroatoms on an atomic level. Time-resolved spectroscopy reveals multiexponential reaction dynamics on the few picoseconds time scale, which are interpreted by quantum chemical calculations at the CASSCF/CASPT2 level of theory. Detailed insight into the processes governing the ultrafast decay from the first excited state, mediated by a number of conical intersections, is provided. Charge separation and charge balance recovery on the reaction pathway play the leading role and are controlled by the electron-donating or -withdrawing character of the heteroatoms. The electronic and geometric structures of the individual minimum energy conical intersections governing the reaction are rationalized, and an extended energetically low lying conical intersection seam is extracted. Comparison to the experimental results permits linking the observed time constants to molecular intermediates and pathways. An explanation is provided for the pronounced differences of Z → E and the E → Z photoreactions upon excitation to the first excited singlet state.

1. Introduction

Time-resolved techniques applied to photoinduced processes represent an ultimate tool for a thorough and detailed study of elementary chemical or physical processes that occur on a molecular level. Ultrashort pulses, of either electromagnetic or electronic nature, can trigger various transitions such as electronic processes (e.g., ionization or charge recombination), chemical transformations (bond cleavage and formation, hydrogen transfer, bond rotation), or phase transitions¹ and monitor them in real time with a resolution down to attoseconds (1 as = 10⁻¹⁸ s). While the kinetics of a distinct (photo)chemical reaction can be resolved with extremely high temporal precision, the molecular and functional interpretation of intermediates and their role for product formation is still missing. However, recent advances in quantum chemistry allow sophisticated theoretical calculations of molecules with increasing complexity. Hence, a combination of (time-resolved) experiments with modern quantum chemical calculations is a promising way for a detailed description of the principles that underlie chemical transformations. The combination of both methods should allow creation of a “molecular movie” of the complete isomerization process.

The molecular system under study, Hemithioindigo (HTI), belongs to a fairly new class of photochromic molecules.^{2–5} The molecular structure of HTI (Figure 1) is based on two different, but well-known, organic compounds, namely thioindigo and stilbene. HTI exists in two different stereoisomers

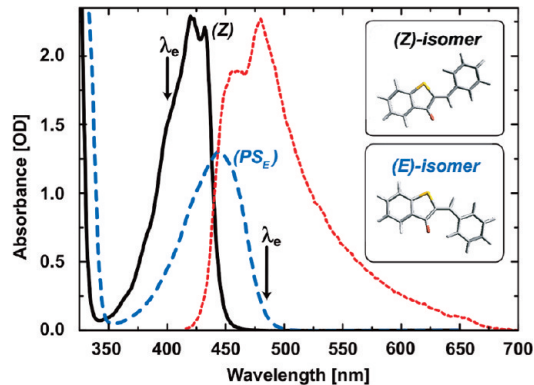


Figure 1. UV/vis spectra of HTI. Absorptions of the Z isomer (solid black line) and PS_E (dashed blue line; photostationary state PS_E containing the isomer E at high (>70%) concentration) together with Z isomer emission (red dashed line) are shown for the nonpolar solvent cyclohexane. The arrows indicate the excitation wavelength λ_e in the time-resolved experiments. Insets: schematic drawings of the two HTI isomers.

(Figure 1, Z and E), which can be interconverted by near-ultraviolet (UV) and visible (vis) light (Figure 1). For our study, we selected HTI as a minimal model for isomerization comprising the following key features: (i) photochromism (see spectra in Figure 1), which facilitates interesting applications;^{6–9} (ii) the possibility of studying the light-induced isomerization with high time-resolution; (iii) HTI as a molecule built from two different parent molecules with well-known properties; (iv) the (moderate) size of the HTI molecule, which allows state-of-the-art quantum chemical calculations; (v) heteroatoms contained in HTI, which offer a wide range of active sites to be functionalized.

* To whom correspondence should be addressed. E-mail: Regina.de_Vivie@cup.uni-muenchen.de.

[†] Department of Chemistry and Biochemistry.

[‡] BioMolecular Optics and CIPSM[‡].

[§] Present address: Department of Physics and Biological Physics Research Group, University of Oxford, Parks Road, Oxford OX1 3PU, U.K.

To distinguish between the individual building blocks and the HTI molecule itself, the following nomenclature was adapted in the present article: the aromatic building blocks are addressed as hemithioindigo and hemistilbene, respectively, whereas the whole molecule is referred to as HTI.

Recently, different experimental studies for differently substituted HTI molecules in polar solvents have been performed and a qualitative picture of both photoreactions $Z \rightarrow E$ and $E \rightarrow Z$ have been published.^{8–11} HTI derivatives have been used as ultrafast molecular switches in biomolecules to initiate structural changes at reasonably high quantum efficiencies.^{7–9} Forward and backward processes in HTI showed significant differences in the reaction dynamics, and there is a strong and systematic dependence on substitution.^{10,11} Recently a theoretical study of HTI¹² was published. Surprisingly, the authors reported fluorescence decay as the dominant pathway contrary to the interpretation given in the context of the experimental investigations.

There are a number of publications on the theoretical description of cis–trans photoisomerizations focusing on either nonpolar or strongly polar compounds. The ultrafast dynamics of the nonpolar basic building block ethylene,^{13–16} its aromatic derivatives styrene¹⁷ and stilbene,^{14,18,19} and linear conjugated hydrocarbons of variable chain length (ref 20 and references in section 4 therein) were studied extensively. As a common feature, similar intermediates such as the triangular kink structure for the conical intersection emerged due to the covalent excited state character. Remarkable research activity has also been documented on the photoisomerization of strongly polar Schiff bases, like the methaniminium cation (CH_2NH_2^+), isoelectronic to ethylene, or its functionalized derivatives^{21,22} (see also ref 20 and references in section 6 therein). Prominent representatives are the chromophores of the rhodopsin, retinal,^{23–27} and of the yellow fluorescent protein, *p*-coumaric acid.^{28–30} It has been shown that due to the molecular charge and its interaction with the protein environment new geometries for the conical intersection such as the one-bond-flip appear.

There are only a few studies on cis–trans photoisomerization reactions for polar neutral molecules involving heteroatoms, focused on small representatives, such as α,β -enones,³¹ β,γ -enones,³² and fluoroethylene.³³ From an electronic point of view polar neutral molecules combine the features of both classes described above. In this paper we study HTI as a complex prototype for Z/E isomerization providing several heteroatoms steering the electron flux by their withdrawing and donating characters. We reduce the complexity of experiments and calculations by focusing on the photochemistry of the simplest possible HTI compound—HTI without any substituents—in a nonpolar environment, i.e., in cyclohexane. We will present the results obtained from ultrafast absorption spectroscopy combined with state-of-the-art quantum chemical methods (CASSCF/CASPT2 for unsolvated molecules) to answer the following questions: (i) What are the reaction coordinates for the isomerization process? (ii) What is the exact geometric and electronic structure of the intermediates along the reaction pathway? (iii) What are the driving forces for isomerization? (iv) Do the heteroatoms influence the choice between the polar and nonpolar reaction pathways? (v) Why do both isomers, Z and E, show such a different isomerization speed?

2. Materials and Methods

2.1. Time-Resolved Spectroscopy. Details of the experiments, either time resolved or steady state, on Hemithioindigo can be found in refs 7–11. HTI as shown in Figure 1 was

synthesized by the group of K. Rück-Braun. The synthesis of HTI derivatives is described in refs 2, 4, 5, and 34–36. HTI was dissolved in cyclohexane (spectroscopic grade, used as received from Sigma Aldrich) for all experiments. Absorption spectra were recorded on a standard absorption spectrophotometer (Perkin-Elmer, Lambda 19); photochemical quantum yields were determined according to ref 7. Fluorescence spectra were recorded on a standard fluorimeter (Specs, Fluorolog 1680, 0.22 m double spectrometer); fluorescence quantum yields were determined as described in ref 37.

All time-resolved transient absorption experiments (TA) were performed on samples at photostationary conditions, with a significant excess (>70%) of the studied isomer (Z or E). For this purpose the millimolar sample solution was illuminated with a mercury–xenon lamp (Hamamatsu Lightningcure LC4 - L8444) in combination with a 3 mm long-pass filter GG395 (Schott) with emission peaks at 400/430 nm) yielding sample PS_E with a high concentration of the E form. A cold light source (KLC2500, Schott, Mainz, filtered by a 3 mm thick GG475 (Schott)) was used for generating high sample PS_Z with an excess of the Z form. The sample solution was pumped through a fused silica cuvette (Hellma) to ascertain defined starting conditions for the femtosecond pump–probe experiments. Ultrashort laser pulses at 800 nm with a pulse duration of ≈ 70 fs at a repetition rate of 1 kHz were delivered from a Spitfire Pro XP (Spectra Physics, Darmstadt) laser system. Pump pulses at the excitation wavelength 400 nm ($Z \rightarrow E$ isomerization) used at an energy of 100–400 nJ were generated by frequency doubling the laser fundamental in a 0.5 mm thick nonlinear β -barium borate crystal (BBO, type I, 29°). Excitation pulses at 485 nm ($E \rightarrow Z$ isomerization) were generated by a noncollinear optical parametric amplifier (NOPA).^{38,39} In the probing process the transient absorption changes $A(\lambda,t)$, induced by the pump pulse were recorded in multichannel fashion using a white light continuum generated in CaF_2 ($\lambda_{\text{probe}} = 350–700$ nm).^{40,41} Pump and probe beams of 100 and 40 μm diameter were spatially overlapped at the sample location with polarization at the magic angle (54.7°). The temporal delay between pump and probe pulses could be varied by a mechanical delay stage. The experimental apparatus was characterized by a time resolution of ≈ 130 fs for 400 nm and ≈ 80 fs for 485 nm excitation. The resulting multidimensional data sets $A(\lambda,t)$ were analyzed according to ref 42.

2.2. Computational Details. The quantum chemical studies were performed with the software packages Molpro rev. 2006.1,⁴³ Molcas rev. 7.4,⁴⁴ and Gaussian 03 rev. D.01.⁴⁵ Excited state structural optimizations were done on the complete active space (CAS) SCF level⁴⁶ including up to 10 electrons and nine orbitals in the active space. For points of interest second order perturbation correction (CASSPT2)^{47–49} was carried out, utilizing 14 electrons and 13 orbitals in the active space. Transition dipole moments were obtained with the CASSCF state interaction (RASSI)⁵⁰ method as implemented in Molcas 7.4. Electrostatic potentials (ESPs)⁵¹ were used to visualize the charge distribution along the reaction path in the ES. For the ES calculations we use the nomenclature SA-*n* and MS-*n* for averaging over *n* states in CASSCF and in CASPT2, respectively. Single state calculations are denoted by SS-CASSCF or SS-CASPT2.

The size of HTI does not allow the inclusion of all π -orbitals in the active space. We considered all first neighbors to the central double bond and one set of bonding and antibonding orbitals per benzene ring on either side (Figure 2). Critical is the role of the oxygen lone pair, which can interact with the

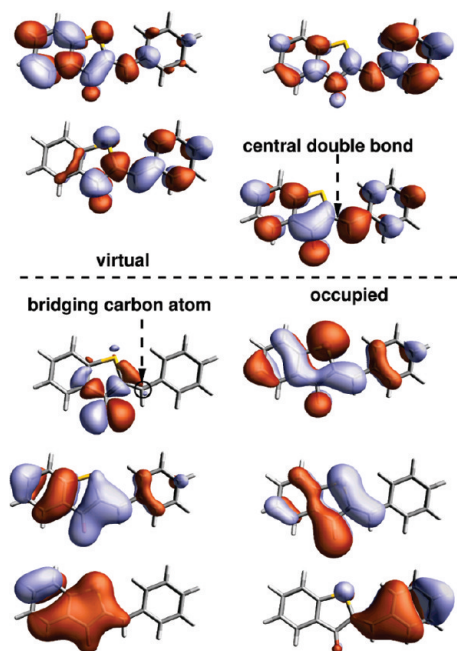


Figure 2. Molecular orbitals of HTI used for the construction of the active space (10 electrons/9 orbitals) plus the oxygen lone pair.

aromatic π -system of the hemistilbene depending on the structural arrangement and in principle must be considered in the active space. However, the simultaneous description of $n\pi^*$ and $\pi\pi^*$ states can lead to well-known problems in CASSCF due to an unbalanced description of the electron correlation. For HTI we followed different strategies to obtain a consistent description of the energetics (for details see section 1.2 in the Supporting Information).

These difficulties are also the origin of the poor excitation energies for $\pi\pi^*$ states in large-scale polyene-type systems and arise from the missing short-range (dynamic) correlation, already documented in the literature.^{52,53} Its neglect can lead to the interchange of excited states, e.g., $n\pi^*$ (with already well described electron correlation) and $\pi\pi^*$ states.⁵⁴ Furthermore, the character of the electronic states and thereby the amount of the correlation energy changes along the minimum energy path and CASSCF can often only provide a qualitative description of the ES topography. Therefore, comparative single point CASPT2(14 electrons/13 orbitals) calculations with Molcas 7.4, using a ionization potential–electron affinity (IPEA) modified zero order Hamiltonian⁵⁵ with an IPEA shift parameter of 0.25 au and a real denominator shift of 0.30 au,^{56,57} were performed at all optimized stationary structures to incorporate the missing electron correlation. The active space was extended by an additional set of bonding and antibonding orbitals per benzene ring to avoid unphysical large contributions from the perturbation treatment.

The stationary structures (minima, transition states, conical intersections) were optimized on the CASSCF level with the standard Pople basis set 6-31G*,^{58–60} and their characters were verified by frequency analysis. A relaxed state averaged scan at CASSCF level along two reactive coordinates was performed for the construction of the two-dimensional (2D) excited state (ES) potential energy surfaces (PES), using the smaller basis set 6-31G. The influence of the oxygen lone pair becomes important in the vicinity of the S_1/S_0 intersection space, and the lone pair orbital was included in the active space in the 2D scan as well as for individual conical intersections using the strategies outlined in section 1.2 in the Supporting Information.

Conical intersections (CoIn) are points of degeneracy between different electronic states and are discussed in section 3.2.2.

Minimum energy CoIn were optimized with the method implemented in Molpro and initially proposed in refs 61 and 62. The variety of CoIn present in HTI required a flexible, individually adapted active space. A CoIn seam was obtained using a three-step procedure. A linear interpolation between two points on the seam (e.g., two minimum energy CoIn) is followed by a constrained CoIn search in the intersection space starting from the interpolated points. Subsequent free optimization along the gradient difference vector is performed as implemented in Gaussian 03. The details are discussed in section 2 in the Supporting Information.

3. Results

3.1. Experimental Results: Stationary and Time-Resolved Absorption Spectroscopy. Previous experiments on the reaction dynamics of HTI investigated the molecules in solvents of high polarity. In order to allow ready comparison with the results from our solvent-free theoretical investigations (see below), we performed the experiments in the nonpolar solvent cyclohexane.

3.1.1. Z → E Photoreaction (400 nm Excitation). Exciting the Z isomer of HTI with near-ultraviolet light at 400 nm immediately results in strong absorption changes. In Figure 3a the time dependence of the absorption change is plotted as a function of time delay between pump and probe pulses for $\lambda_{\text{pr}} = 437$ and 573 nm. At time zero there is (at 573 nm) a strong rise of the absorption. A weak decay on the time scale of 2 ps is followed by a strong decrease in absorption on the 10 ps time scale. At 437 nm a rise in absorption is found on the time scale of 600 ps. At 573 nm a very weak absorption decrease is found at late delay times. Absorption spectra taken at different delay times are shown in Figure 3b. They are important for the molecular interpretation of the observed transients. At early times, one observes the formation of a broad and structured absorption change throughout the investigated spectral range (Figure 3b, 0.2 ps). The absorbance change is characterized by peaks at 450 and 550 nm, and a minimum at 425 nm. The absorption increase can be assigned to excited state absorption (ESA), which is overlapped by negative signal contributions arising from ground state (GS) bleaching (centered at 425 nm) and stimulated emission (SE) centered at 490 nm. The spectral positions, from both GS bleaching and SE, are in good agreement with stationary spectra of HTI in the nonpolar solvent cyclohexane (Figure 1 and refs 3 and 5). On the time scale of a few picoseconds minor changes of the peak positions and the oscillator strength of ESA/SE can be observed (Figure 3b, 0.2 ps vs 2.0 ps). The dominant decay of the induced absorption signal is seen on the time scale of 10 ps (Figure 3b, 2.0 ps vs 12 ps). After this decay a broad absorption band with a slight maximum at 450 nm and bleaching at 425 nm can be observed (Figure 3b, 25 ps). It is only after hundreds of picoseconds that most of the remaining induced absorption (>450 nm) decays and reveals the difference spectrum expected from the formation of the E isomer.

Global fitting of the data set by a multiexponential model (using three time constants together with an offset) and the inspection of the transient spectra (see Figure 3b) allow interpretation of the data with the scope of recently established reaction models.⁶³ There is a first kinetic component ($\tau_0 = 2.0 \pm 0.8$ ps) connected with weak absorption changes. The small changes in absorption indicate that this kinetic component may be caused by reactions in the excited electronic state. Interestingly, changes of the SE during this first reaction are much

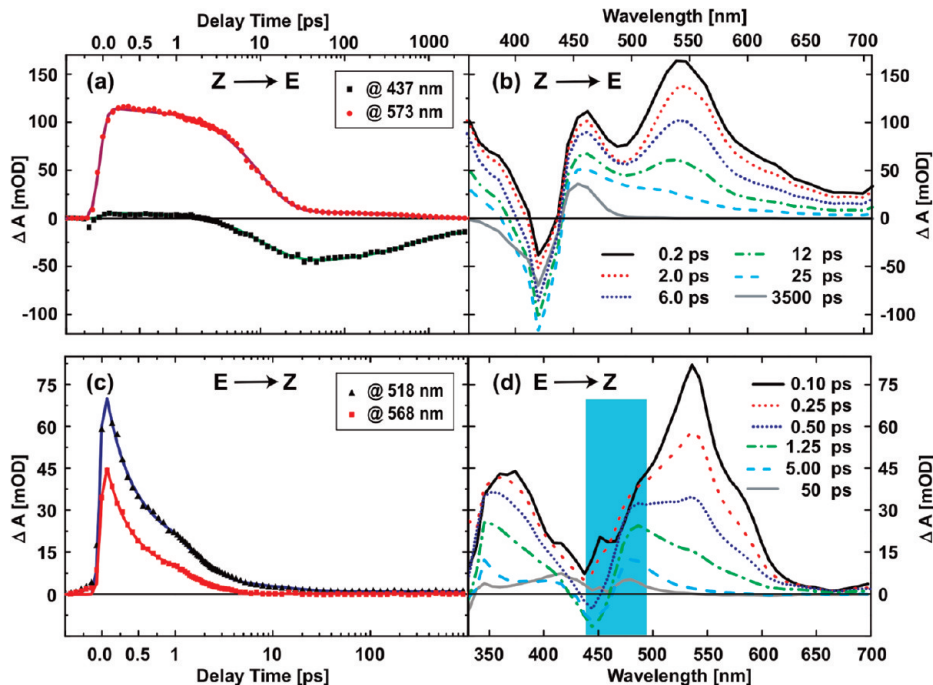


Figure 3. Results from transient absorption spectroscopy. (a and b) $Z \rightarrow E$ isomerization after 400 nm excitation. (a) Time-dependent absorption change measured as a function of delay time for probing at 437 and 573 nm. (b) Transient spectra at certain delay times between pump and probe pulse. (c and d) $E \rightarrow Z$ isomerization after 485 nm excitation. (c) Time-dependent absorption change recorded as a function of delay time for probing at 518 and 568 nm. (d) Transient spectra at certain delay times between pump and probe pulse. In the range of probing wavelengths marked in blue the accuracy of the absorption measurement is reduced due to stray light from the excitation pulse.

weaker than the ones observed recently for HTI in more polar solvents such as dichloromethane¹⁰ or methanol.^{7,9} Subsequently, one finds the second kinetic component (time constant of $\tau_1 = 10 \pm 1$ ps) with a much stronger absorption signal representing the decay of the ES and the transition into the GS (of the educt Z and the product E). This interpretation is supported by the observed decay of ESA and SE and the appearance of the absorption peak at 450 nm corresponding to the product isomer.

At late delay times we find a very slow component $\tau_2 = 650 \pm 200$ ps related to the decay of a broad absorption band extending from <400 to >600 nm and the superimposed recovery of GS bleach at 425 nm. We tentatively assign this transition to the decay of a short-lived triplet state. The photochemical conversion efficiency $\phi_{pc,Z}$ of the $Z \rightarrow E$ process was measured in stationary experiments in the weakly polar solvent dichloromethane and was found to be $\phi_{pc,Z} = 0.230 \pm 0.035$. An alternative assignment of the 650 ps kinetic component to the decay of the excited electronic singlet state can be ruled out by the following observations. One finds a very small fluorescence quantum yield of HTI in cyclohexane of $\phi_{fl} = 0.0003$ and a rather long radiative lifetime of $\tau_{rad} = 15$ ns (obtained from the Strickler–Berg relation⁶⁴). As a consequence, the fluorescing excited electronic state should have a livetime τ_{S1} in the range of $\tau_{S1} \approx \tau_{rad}\phi_{fl} = 4.5$ ps. This finding gives clear evidence that the slow kinetic component $\tau_2 = 650 \pm 200$ ps is not associated with a (fluorescent) singlet state populated for the major fraction of the molecules.

3.1.2. $E \rightarrow Z$ Photoreaction. The transient absorption changes induced by excitation at 480 nm of the E isomer are shown in Figure 3c,d. The time dependence observed at two probing wavelengths (518 and 568 nm, Figure 3c) reveals very fast reaction dynamics. This increased reaction speed is also visible in the transient spectra shown in Figure 3d. Immediately after excitation there are features from ESA and GS bleaching (Figure 3d). First absorption transients occur on the 100 fs time

scale (see Figure 3c) and are followed by a 1 ps process. Subsequently a weak absorption change is visible on the 10 ps time scale. We do not find any indication for a transient in the 100 ps range. A multiexponential modeling of the transients yields time constants of $\tau_0 = 260 \pm 80$ fs, $\tau_1 = 1.2 \pm 0.4$ ps, and $\tau_2 = 13 \pm 6$ ps. With the molecular model proposed for other HTI molecules⁶³ we assign the 260 fs process to the initial motion on the excited electronic potential surface, the 1.2 ps transient to the transition from the ES to the GS of educt and product, and the 13 ps process to vibrational cooling of the reformed E isomer. The photochemical yield for Z -product formation was determined in dichloromethane to be only $\phi_{pc,E} = 0.053 \pm 0.016$.

In the following sections the combination of experimental data on our minimal molecular model—HTI in an nonpolar solvent—with state-of-the-art theory opens the pathway to a detailed insight into the pure molecular driving forces for Z/E isomerization.

3.2. Theoretical Results. 3.2.1. Vertical Excitation from Both Isomers. The GS equilibrium structures of both isomers characterize the initial and the final states of the photoreaction and were optimized at the DFT level of theory with the B3LYP hybrid functional,^{65–67} which has proved to be reliable for ground state problems. Both isomers were found to be planar, i.e., of C_S symmetry (Figure 1). At the SS-CASSCF(14/13) level the lowest excited electronic state corresponds to a $n \rightarrow \pi^*$ excitation from the oxygen lone pair (Figure 2) into the aromatic system (Table 1). In C_S symmetry this state has no oscillator strength. Only by symmetry-breaking motions may some oscillator strength be borrowed. The second ES is a $\pi \rightarrow \pi^*$ transition with a transition dipole moment of 2.39 D for Z -HTI and of 2.10 D for E -HTI.

The excitation energies for the $\pi \rightarrow \pi^*$ transition of 4.67 eV (Z isomer) and 4.39 eV (E isomer) deviate significantly from

TABLE 1: Vertical Excitation Energy $\Delta_{S_0-S_N}$, Transition Dipole Moment, and ES Electronic Character at the FC Points of Z- and E-HTI^a

	SS-CASSCF(14,13)			SS-CASPT2(14,13)			expt $\Delta_{S_0-S_N}$ (eV)	
	$\Delta_{S_0-S_N}$ (eV)	$\langle S_N \mu S_0 \rangle$ (D)	character	$\Delta_{S_0-S_N}$ (eV)	$\langle S_N \mu S_0 \rangle$ (D)	character		
Z	S ₁	3.75	0.00	nπ*	3.48	2.75	ππ*	2.92
	S ₂	4.67	2.39	ππ*	3.72	0.00	nπ*	—
E	S ₁	3.57	0.00	nπ*	3.27	2.44	ππ*	2.76
	S ₂	4.39	2.10	ππ*	3.60	0.00	nπ*	—

^a Transition dipole moments are derived from the oscillator strength f at SA-2-CASSCF(14,13) level according to $\langle S_N | \mu | S_0 \rangle = [3f/(2\Delta E_{S_0-S_1}^{\text{CASPT2}})]^{1/2}$. ^b Active space generated by exchanging the 3p_z orbital of sulfur by the oxygen lone pair (Figure 2).

the experimental values (see absorption spectra in Figure 1) with maxima at 2.92 and 2.76 eV, respectively.

Perturbative correction (section 2.2) recovers more than 60% of the missing dynamic electron correlation energy of the ππ* state, which becomes the lowest ES at the SS-CASPT2 level with excitation energies corrected to 3.48 and 3.27 eV. Comparable calculations at the time-dependent DFT (TDDFT) level confirm this energetic order.¹² However, the shortcomings of TDDFT in describing double excitations, as well as the overestimation of charge transfer states, which gain in importance away from the Franck Condon (FC) region, prevent its use for the description of the complete ES reaction path.

Based on the state order predicted by SS-CASPT2, we assume that upon laser irradiation the electron is excited into an S₁ state of ππ* character. Furthermore, we find that the ππ* and nπ* states are very close in the FC region (energy separation ~0.3 eV) and one can speculate on a partial excitation of the nπ* state by femtosecond pulses opening reaction channels, which compete to the direct S₁ relaxation pathway.⁶⁸ Experimental indications are found in the long time constant $\tau_2 = 650 \pm 200$ ps, tentatively attributed to triplet contributions. Preliminary calculations support the existence of a side channel trapping the molecule in a dark nπ* region on S₁ from where it can decay

via intersystem crossing similar to the singlet–triplet pathway discussed by M. Reguero et al. for the structurally related acrolein.³¹

3.2.2. Fundamental Considerations on the Electronic Structure of Conical Intersections. The isomerization of HTI is a typical example of an ultrafast photoreaction proceeding on a picosecond time scale. Its ES decay cannot be explained by means of the avoided crossing model of van der Lugt and Oosterhoff^{69,70} applying Fermi's golden rule,⁷¹ nor by fluorescence from stable ES intermediates. Exclusion of the radiative decay of the ES as a major decay path to the GS is supported by the low fluorescence quantum yield $\phi_f = 0.0003$ (section 3.1). It is therefore obvious to assume a CoIn-gated decay model that manages to explain both the ultrafast time scale and the suppressed fluorescence.

CoIn are critical features of the reaction profile. They constitute points of degeneracy between two (or more) PES and facilitate a rapid radiationless decay to the lower lying state. With the ongoing development of computational methods, the search in the degeneracy space, called the intersection space (IS),⁷² for energetically low lying crossings has become possible.^{31,73–75} Studies by Bernardi, Garavelli, Olivucci, and Robb revealed that a number of minimum energy CoIn are characterized by common two-, three-, and four-center patterns.^{20,76,77} The fundamental work of Michl and Bonačić-Koutecký shed light on the electronic structure of the IS^{23,78} between GS and ES in linear conjugated systems. The torsional deformation about a double bond leads to the degeneracy of the π and π* orbitals and to the formation of an S₁/S₀ avoided crossing (Figure 4a). As a consequence the π and π* orbitals transform into orbitals denoted “A” and “B” that localize on either side of the central double bond (Figure S3 in the Supporting Information). Occupation of these orbitals leads to the following configurations: a covalent electronic structure |AB⟩ (i.e., both valence electrons are spatially separated, also denoted “dot–dot”⁷⁸) and two zwitterionic states |A²⟩ and |B²⟩ (i.e., both valence electrons occupy the same localized molecular orbital (MO), also denoted “hole pair”⁷⁸). In most cases the covalent electronic structure |AB⟩ is favored and CoIn emerge

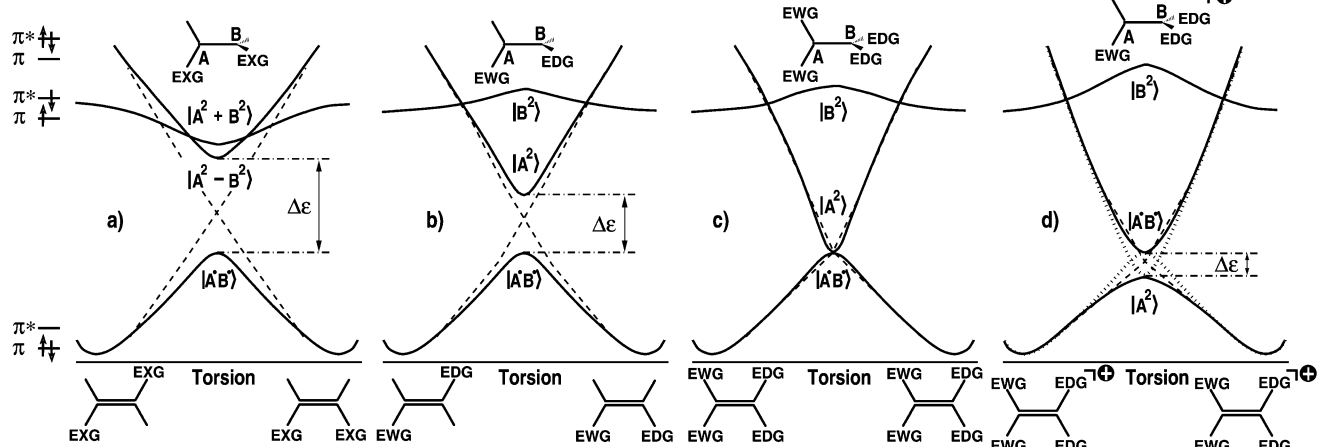


Figure 4. Correlation diagram of the S₀, S₁, and S₂ states during the cis–trans isomerization in differently substituted ethylene derivatives. A representation similar to Figure 13 in ref 78 is used. In the region around 90° a localized basis (A,B) provides a more comprehensible description of the emerging covalent and zwitterionic configurations. (a) Equivalent substitutions on both sides of the double bond (EXG) yield potential curves resembling the ones in the unsubstituted system (homosymmetric biradical). (b) Asymmetric substitution (EWG, electron-withdrawing groups; EDG: electron-donating groups) alters the electronic affinity on both sides of the double bond. The latter leads to the formation of pure zwitterionic S₁ (|A²⟩) and S₂ (|B²⟩) states (also known as “hole-pair” states) besides the covalent S₀ (|AB⟩) state (also known as the “dot–dot” state). Appropriate substitutions can stabilize either one of the zwitterionic configurations (weakly heterosymmetric biradicaloid). (c) Tuning of the properties of the substituents can induce a CoIn without the need of additional geometric adjustments (critically heterosymmetric biradicaloid). (d) In the case the zwitterionic configuration becomes more stable than the covalent one, the S₀ and S₁ states switch characters (strongly heterosymmetric biradicaloid). Protonated Schiff bases are an example of such situation.

when this covalent GS is destabilized and degenerates with the ES. For the present discussion we postulate that the ES has a $|A^2\rangle$ configuration.

Degeneracy can be reached in different ways. In conjugated hydrocarbons (ethylene, stilbene, etc.) geometric deformations in the backbone form hula-twist^{79–82} type CoIn (also known as $-(CH_3)_3-$ kinks^{13,14,75,77,83–86}) that aim to recover the charge balance in the ES $|A^2\rangle$ by transferring electron density from the doubly occupied orbital A to the empty orbital B (e.g., hydrogen anion transfer at CoIn_{min} of ethylene^{18,87}). The major change is an energy increase of the covalent GS due to the repulsive electronic interactions during the $-(CH_3)_3-$ kink formation, whereas the ES energy is only slightly lowered. Here the stabilizing effects from the charge balance recovery are compensated by the geometric deformations needed. These CoIn have a nonpolar character and their locus coincides with ES minima in the gas phase and in nonpolar solvents. Polar solvents, in contrast, can stabilize the avoided crossing with the zwitterionic configuration $|A^2\rangle$ to a global minimum,³⁰ destabilizing the nonpolar CoIn. Compounds which are likely to form such CoIn are called weakly heterosymmetric biradicaloids⁷⁸ (Figure 4b) or homosymmetric biradicals in the more specific case of equivalent substituents on both sides of the double bond (Figure 4a).

The second possible way of reaching a degeneracy between GS and ES is the exchange of carbon atoms from the backbone with heteroatoms or the introduction of appropriate polar substituents. Hereby mesomeric and inductive effects can stabilize the zwitterionic state $|A^2\rangle$. If these effects are strong enough, the degeneracy with the covalent GS $|AB\rangle$ can be reached without unfavorable geometric deformations (Figure 4c). Compounds able to form such polar type CoIn are referred to as critically heterosymmetric biradicaloids.⁷⁸

In the extreme the zwitterionic configuration can be stabilized below the covalent state. This situation is found in some protonated Schiff bases (Figure 4d) where the one-bond-flip (OBF)^{77,88–91} CoIn drives the cis–trans isomerization. The positive charge at the nitrogen increases its electron affinity dramatically so that at 90° torsion the zwitterionic $|A^2\rangle$ configuration (with A localized at the side of the nitrogen) becomes more stable than the covalent configuration. Such compounds are called strongly heterosymmetric biradicaloids.⁷⁸ From Figure 4c,d it becomes obvious that polar CoIn coincide with the global minimum on the ES PES (“sand in the funnel” picture)²¹ independent of the polarity of the solvent.

Analogous considerations are valid for further types of reactions following the van der Lugt/Oosterhoff model, such as electrocyclic reactions.^{73,92,93} We will show in the following sections that HTI is a model compound in which both a cis–trans isomerization and an electrocyclic reaction compete, involving heteroatoms as decisive factors.

3.2.3. Variety of Stationary Conical Intersections for HTI.

The search for CoIn in HTI reveals a multitude of different species. Figure 5 shows a representative set of CoIn geometries, all of them local minima in the S_1/S_0 IS. Their corresponding highest occupied molecular orbitals (HOMOs) and lowest unoccupied molecular orbitals (LUMOs) are provided in Figure S4 in the Supporting Information. Table 2 summarizes their geometric and energetic characteristics. Several CoIn are of nonpolar type (CoIn_{HT} , CoIn_{Et} , CoIn_S , their diastereomers $\text{CoIn}_{\text{HT}*}$, $\text{CoIn}_{\text{Et}*}$ (not shown in Figure S4 in the Supporting Information), and CoIn_{S^*} as well as CoIn_{Ac}) and one is of polar type (CoIn_{CHD}). From the discussion in section 3.2.2, we can deduce that HTI behaves like a weakly heterosymmetric

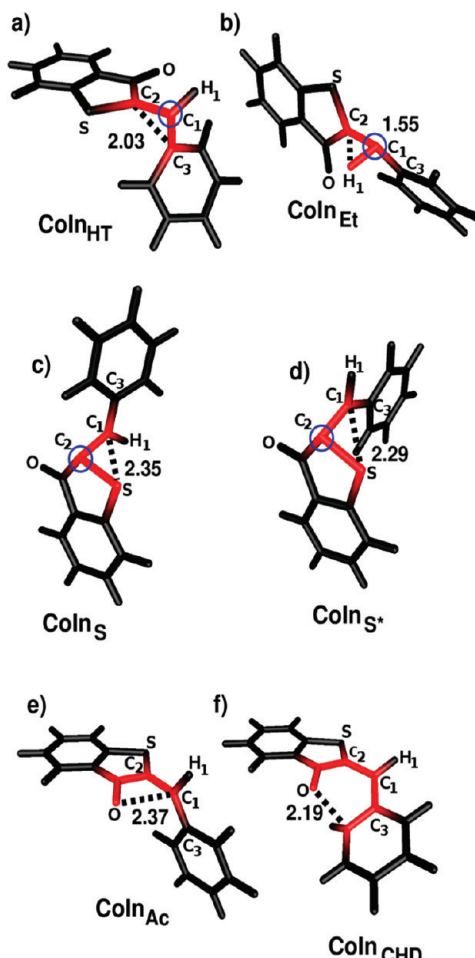


Figure 5. Geometries for selected CoIn of HTI. The subscripts symbolize the characteristic geometric arrangements (marked in red), obtained for the individual CoIn: HT stands for hula-twist; Et stands for ethylene; Ac stands for acrolein; CHD stands for cyclohexadiene; S and S^* indicate that a sulfur atom is involved in the CoIn kink. Carbon atoms exhibiting pyramidalization during CoIn formation are marked with a blue circle.

biradicaloid at the nonpolar CoIn and like a strongly heterosymmetric biradicaloid at CoIn_{CHD} . All structures, except CoIn_{CHD} , exhibit among other deformations a distinct 90° torsion around the central double bond required for cis–trans isomerization. CoIn_{CHD} opens a major decay channel to the GS, however, not for the isomerization, as elucidated later.

At 90° torsion the ES electron density in the frontier orbital is localized on the hemithioindigo. The system strives to stabilize this unfavorable charge concentration. Different ways to recover the original charge balance are realized at the various CoIn. In common they all require two additional motions: a pyramidalization and a tilting between both aromatic motifs. All three motions happen simultaneously to reach the individual CoIn. The separation into submotions serves the analysis of the relaxation process and the comparison of the different solutions realized at the CoIn.

At CoIn_{HT} and CoIn_{Et} the pyramidalization occurs at the carbon atom C_1 (marked with a blue circle) bridging both aromatic sides of HTI. With progressing pyramidalization the electron density first switches completely to the hemistilbene and only then the charge balance is achieved by bringing both aromatic motifs closer via the tilting motion. For CoIn_{HT} the tilting motion shortens the distance between C_2 and C_3 (Figure 5a) to 2.03 Å, establishing the bridge for the electron flow. At

TABLE 2: Δ_{S_0} , Δ_{S_1} , and $\Delta_{S_0-S_1}$ at SA-2-CASSCF(10/9) and MS-2-CASPT2(14/13) Levels, Reactive Coordinates, and Transition and ES Permanent Dipole Moments at SA-2-CASSCF(10/9) Level for All Points of Relevance^{a,b}

structure	SA-2-CASSCF (10/9)			MS-2-CASPT2 (14/13)			reactive coordinates			dipole moments		
	Δ_{S_0} (eV)	Δ_{S_1} (eV)	$\Delta_{S_0-S_1}$ (eV)	Δ_{S_0} (eV)	Δ_{S_1} (eV)	$\Delta_{S_0-S_1}$ (eV)	$C=C^c$ (Å)	torsional (deg)	pyramidal. (deg)	tilt (deg)	$\langle S_1 \mu S_0 \rangle$ (D)	$\langle S_1 \mu S_1 \rangle$ (D)
FC _Z	0.00	0.00	4.79	0.00	0.00	3.59	1.35	0.0	0.0	—	2.75	6.23
FC _{Z*}	0.36	-0.41	4.02	0.50	0.04	3.13	1.41	0.0	0.0	—	1.88	7.30
Min _{S1Z}	0.70	-0.43	3.65	0.78	0.02	2.84	1.42	29.4	13.1	—	1.76	6.84
TS _{S1Z}	1.15	-0.43	3.19	1.21	0.04	2.42	1.44	43.0	21.3	—	1.87	6.03
TS _{S0}	2.18	-0.59	2.01	2.03	0.26	1.83	1.47	90.0	1.8 ^d	0.0 ^d	0.03	11.04
CoIn _S	3.80	-0.99	0.00	3.44 ^e	-0.15 ^e	0.49	1.44	90.0	64.0 ^d	18.6 ^d	1.38	5.76
CoIn _{S*}	4.58	-0.49	0.00	3.83 ^e	0.24 ^e	0.31	1.45	90.0	-59.0 ^d	21.7 ^d	1.90	4.26
CoIn _{Ac} ^{f,g}	3.07	-1.71	0.00	3.37 ^e	-0.22 ^e	0.03	1.48	90.0	0.6 ^d	-19.1 ^d	0.56	1.49
CoIn _{CHD}	3.03	-1.75	0.00	2.93 ^e	-0.66 ^e	0.48	1.44	154.9	3.0 ^d	—	0.13	1.50
CoIn _{HT} ^f	5.16	0.37	0.00	5.13 ^e	1.53 ^e	0.07	1.46	90.0	59.6 ^h	23.3 ^h	0.42	2.27
CoIn _{HT*} ^{f,g}	5.60	0.81	0.00	5.15 ^e	1.56 ^e	0.21	1.44	90.0	-57.0 ^h	19.4 ^h	1.18	3.61
CoIn _{Ei} ^{f,i}	4.52	-0.27	0.00	4.86 ^e	1.26 ^e	0.06	1.39	90.0	54.1 ^h	-28.0 ^h	1.22	3.62
CoIn _{Ei*} ^{f,i}	4.60	-0.19	0.00	4.96 ^e	1.36 ^e	0.04	1.39	90.0	-52.5 ^h	-28.5 ^h	0.41	4.85
TS _{S1E}	1.36	-0.36	3.00	1.39	0.03	2.24	1.45	136.4	-15.4	—	2.13	4.02
Min _{S1E}	0.61	-0.44	3.74	0.70	0.01	2.91	1.42	180.0	0.0	—	1.69	7.44
FC _E	0.24	-0.03	4.51	0.22	-0.03	3.34	1.36	180.0	0.0	—	2.37	6.30

^a Δ_{S_0} , relative GS energy (with respect to the equilibrium structure of Z-HTI), Δ_{S_1} , ES energy (with respect to the FC point of Z-HTI on S₁); $\Delta_{S_0-S_1}$, vertical excitation energies. ^b Transition dipole moments derived from the oscillator strength f given by Molcas7.4, according to $\langle S_N | \mu | S_0 \rangle = [3f/(2\Delta E_{S_0-S_1}^{CASPT2})]$ with ΔE in au. ^c Central double bond as denoted in Figure 2. ^d Tilt and pyramidalization defined with respect to C₂ (see Figure 5c–f and Figure S.1 in the Supporting Information). ^e Δ_{S_0/S_1} evaluated using an averaged value for the MS-2-CASPT2 energy at the particular point, i.e., $(E_{S_1} + E_{S_0})/2$. ^f Optimized without the sulfur 3p_z orbital. ^g Optimized including the oxygen lone pair in the active space (Figure 2). ^h Tilt and pyramidalization defined with respect to C₁ (see Figure 5a,b and Figure S.1 in the Supporting Information). ⁱ Optimized including the C₁–H₁ σ - and σ^* -orbitals in the active space.

CoIn_{Ei} the hemistilbene group is differently oriented and the charge balance is achieved via the H₁ and C₂ interaction (Figure S4 in the Supporting Information). For a proper description the σ_{CH} and σ^*_{CH} orbitals were included in the active space. The resulting formation of a triangular kink among three carbon atoms (CoIn_{HT})⁸² or two carbon atoms and one hydrogen (CoIn_{Ei})¹⁴ is typical for nonpolar CoIn. CoIn_{HT} resembles the well-known hula-twist arrangement mediating, for example, the stilbene cis–trans isomerization,^{13,82} whereas CoIn_{Ei} is the analogue to the minimum energy CoIn of ethylene.^{14,18,19}

CoIn_S is geometrically related to CoIn_{HT} and CoIn_{Ei}, except that the pyramidalization occurs at the carbon atom C₂ of the hemithioindigo (marked with a blue circle in Figure 5c). This pyramidalization favors an effective S–C₁ interaction via their p_z orbitals, and the charge balance can be directly reached without the additional shift of electron density observed at CoIn_{HT} and CoIn_{Ei}. All three CoIn possess diastereomeric structures for 180° torsion around the central double bond with slightly different characteristics due to the asymmetry in the molecule. Exemplarily, CoIn_{S*} is shown in Figure 5d.

CoIn_{Ac} requires no pyramidalization. Here, the favorable orientation of the oxygen lone pair toward the 2p_z orbital of the bridging C₁ atom opens another possibility for direct charge balance recovery by a tilting motion, visible in the short C₁–O distance. For an appropriate description, we included the lone pair of the oxygen in the active space. CoIn_{Ac} has no analogue among conjugated hydrocarbons due to the missing heteroatom. Similar CoIn have been reported for acrolein³¹ and salicylic acid,^{94,95} both enclosing a R₂C=CR–RC=O motif.

The functionality of the polar type CoIn_{CHD} is different. The torsion is only carried out to 30°, and thus, the charge localization observed for the non polar type CoIn does not take place. Both frontier orbitals involve atoms of both aromatic halves, thereby keeping the aromaticity. As a further consequence the GS Z isomer is unlikely to be formed. The structure of CoIn_{CHD} is typical for cyclohexadiene derivatives with strongly polar groups and has been reported for fulgides⁹² and

spiropyrans.⁹⁶ It emerges due to a conrotatory motion. Along this coordinate the frontier orbitals localize as A and B orbitals—in the spirit of Figure 4—at several but different centers of the six-membered-ring moiety (Figure S3 in the Supporting Information). As the oxygen heteroatom participates directly in the 6π ring, it strongly stabilizes only one of the localized orbitals and thereby the zwitterionic configuration. The degeneracy is reached without further structural deformations (Figure 4d).

Next we discuss the relative stability of the individual CoIn.⁹⁷ CoIn_{HT}, CoIn_{HT*}, CoIn_{Ei}, and CoIn_{Ei*} lie above the FC limit at SA-2-CASSCF as well as at MS-2-CASPT2 level (Table 2). Their strong deformations in pyramidalization and tilt and, as revealed by the inspection of the submotions, the additional induced charge transfer render them inaccessible from the S₁ FC region. These four CoIn are not further considered. CoIn_S, CoIn_{S*}, CoIn_{Ac}, and CoIn_{CHD} are energetically accessible from the FC point. Their structures are favored as they support the direct charge balance using the donating effects of the heteroatoms. Of all four, CoIn_{S*} is the energetically highest due to the sterically unfavorable alignment of the hemistilbene and the hemithioindigo. CoIn_S lies about 0.5 eV below CoIn_{S*}. CoIn_{CHD} is the global minimum at the SA-2-CASSCF(10/9) and MS-2-CASPT2(14/13) level, verifying the prediction for polar type CoIn (Figure 4d). The energetic position of CoIn_{Ac} is sensitive to the dynamic correlation effects through the notable nπ* contributions in the ES wave function and differs significantly at the CASSCF and CASPT2 levels. While SA-2-CASSCF predicts an energy in the range of CoIn_{CHD}, at the MS-2-CASPT2 level CoIn_{Ac} lies slightly above CoIn_S. Hence, neglect of the dynamic correlation effects would overestimate the weight of CoIn_{Ac} in the decay process to the GS. The energetic position of the nonpolar CoIn_S and CoIn_{Ac} confirms the qualitative rule that nonpolar CoIn arise mainly through destabilization of the electronic GS. In the gas phase they coincide with local minima on the ES surface.

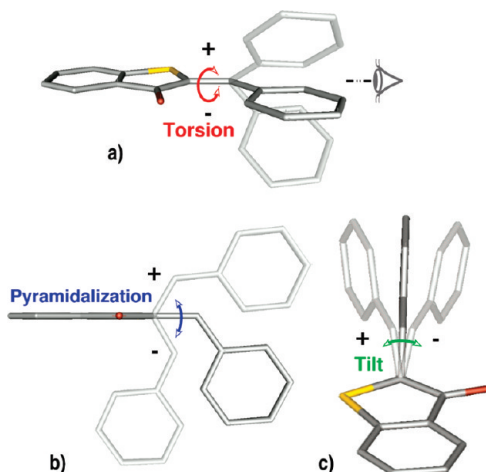


Figure 6. Reactive coordinates used to visualize Z/E isomerization. (a) Out-of-plane torsion with Z-HTI as a zero-point reference [0°:360°]. (b) Pyramidalization shown for a torsional angle of 90° [-90°:+90°]. (c) Tilt shown for a torsional angle of 90° and pyramidalization of +60° [-90°:+90°]. For the choice of reference structure with 0° tilt the reader is referred to the Supporting Information.

3.2.4. Reactive Coordinates and Relaxation on the Excited State Surface S_1 . We derived a set of reactive coordinates (Figure 6) well suited to describe the relaxation from the FC point to the energetically reachable degeneracy region. The out-of-plane torsion of the hemistilbene with respect to the hemithioindigo (Figure 6a) is the main reaction coordinate. We chose the Z-isomer GS equilibrium structure as reference geometry with a torsional angle of 0° and investigated the clockwise Z → E isomerization (0° → 180°), as well as the counterclockwise E → Z isomerization (180° → 0).⁹⁸ The pyramidalization is defined as the out-of-plane bending of the hemistilbene shown in Figure 6b for a reference structure with a torsional angle of 90°. At 0° pyramidalization the bridging carbon atom C₁ lies in the plane of the hemithioindigo. The third coordinate (Figure 6c) is the tilt of the hemistilbene either toward the carbonyl group (negative tilt) or toward the sulfur (positive tilt). The tilt coordinate plays a role only for a torsion of 90° (for details on the construction and the choice of reference structure, see section 1.1 in the Supporting Information). A similar set of coordinates has been used for studies of ethylene^{19,86} and stilbene,¹⁴ varying slightly in the interpretation of pyramidalization and tilt.

Optimizations conserving the C_s symmetry of the GS isomers were performed on the $\pi\pi^*$ S_1 surface starting at their FC points. The calculations were carried out with the (10/9) active space (Figure 2) without state averaging (i.e., SS-CASSCF(10/9)), neglecting the lone pair of oxygen and thereby suppressing the $n\pi^*$ state. In each case the initial relaxation leads to a rearrangement of bond lengths. The central C=C bond is elongated and loses its double bond character, in response to the partial promotion of electron density into the antibonding π^* orbital. Simultaneously, the ES is stabilized by ~0.45 eV for both isomers. On the E-HTI side the planar relaxed geometry coincides with a local minimum (Min_{S1E}). On the Z-HTI side the optimized planar structure (FC_{Z*}) is a transition state (TS). Normal mode analysis reveals an imaginary mode of combined torsional and pyramidalizational deformations, enabled by the weakened central double bond. Unconstrained optimization yields a local minimum (Min_{S1Z}) at 29.4° torsion and 13.1° pyramidalization (Table 2). Stabilization of only 0.02 eV between the FC_{Z*} and Min_{S1Z} is evidence for the extremely flat potential in the torsion–pyramidalization plane. A MS-2-

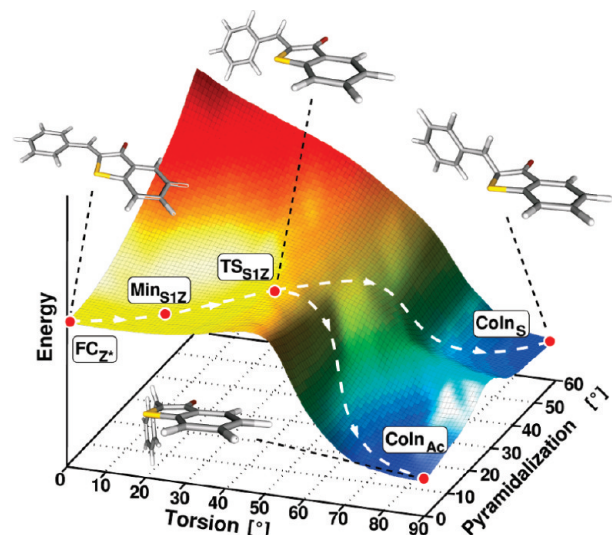


Figure 7. S₁ PES for the Z → E reaction from a 2D relaxed scan in the region of 0°–90° torsion and of 0°–60° pyramidalization. Approximate ES reaction pathways are derived from the topography of the PES (dashed white lines).

CASPT2(14/13) correction to the ES energy confirms the shallow landscape in the torsion–pyramidalization plane.

3.2.5. Potential Reaction Pathways from the ES Minima. An SA-2-CASSCF(10/9) relaxed 2D scan with adaptive active space along the coordinates torsion and pyramidalization was carried out to identify possible reactive pathways from the local minima on the ES to the CoIn. The third reactive coordinate, the tilt, plays a role only in the IS. The corresponding PES are shown in Figure 7 (Z → E) and Figure 12 (E → Z). They are solely of a qualitative nature⁹⁹ as the active space is not uniform for all geometries due to the $n\pi^*-\pi\pi^*$ problem. As described in section 3.2.1, on the CASSCF level the electron correlation in the $n\pi^*$ state is favored compared to the $\pi\pi^*$ state, leading to an inverted energetic order in the FC region, preventing their simultaneous correctly balanced description. However, nonnegligible $n\pi^*$ contributions are present in the vicinity of CoIn_{Ac} (section 3.2.4) requesting the inclusion of the oxygen lone pair in the active space. In principle the unbalanced description of the electron correlation could be remedied by CASPT2 (section 3.2.1). However, this is not affordable for a 2D scan. A consistent picture of the 2D PES is obtained on the CASSCF level following the procedure outlined in section 1.2 in the Supporting Information and including PT2 corrections locally in the vicinity of CoIn_{Ac}.

3.2.5.1. Z → E Potential Energy Surface. The ES PES for the Z → E reaction are plotted in Figure 7 between 0° and 90° torsion and between 0° and 60° pyramidalization. Per construction the torsion runs clockwise (Figure 6a). The starting point at 0° torsion and 0° pyramidalization corresponds to the C_s -symmetric relaxed structure FC_{Z*}. In agreement with the unconstrained optimization, the 2D scan confirms the existence of a local nonplanar minimum, i.e., the Min_{S1Z} on a shallow surface. An SS-CASSCF(10/9)/6-31G* transition state search in the region around 40° torsion and 20° pyramidalization of the ES was carried out to refine its position. The located TS (TS_{S1Z}) is characterized by an imaginary frequency of -43.73 cm^{-1} that points toward CoIn_S. The TS_{S1Z} geometry (structure and normal mode included in the Supporting Information) is shifted with respect to Min_{S1Z} to larger torsion (43.0°) and pyramidalization angles (21.3°). The barrier height is calculated to be less than 1.0 kJ/mol at the CASSCF level and ca. 1.5 kJ/mol at the CASPT2 level, again indicating a very flat landscape.

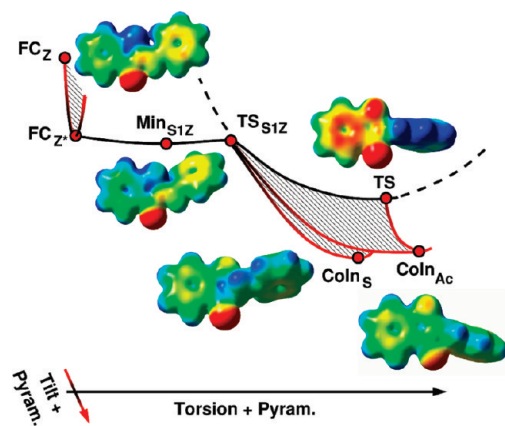


Figure 8. Cut through the S_1 PES with electrostatic potentials for relevant points along the S_1 PES in nonpolar solvents or gas phase, projected on the 0.01 electron bohr $^{-3}$ isodensity surface. Regions with high proton affinity are in red, regions with low proton affinity are in blue. For optimal contrast ratio a minimum value of -0.05 au and a maximum value of 0.15 au were used (1 au = 27.2116 eV). The zwitterionic structure emerging with the torsional deformation cannot be stabilized in the absence of a polar solvent and becomes a TS on the S_1 PES.

3.2.5.2. Electron Density Fluctuation. The flux of electron density in the valence orbitals, identified as one major driving force for CoIn formation is already initiated in the excitation step. For the planar geometries the charge is partially shifted from the hemithioindigo to the hemistilbene and remains there between 0° and 40° torsion (Figure 8). Correspondingly, the permanent dipole moment is increased. After the TS_{S1Z} is passed, the doubly excited π^{*2} configuration mixes in the S_1 wave function (Figures 4 and 7). With ongoing torsion the delocalization breaks down completely (Figure 8, TS) and the electron density of the HOMO now localizes on the hemithioindigo, resulting in a large permanent dipole moment (Table 2). As expected from the one-dimensional (1D) correlation diagram (Figure 4a,b in section 3.2.2), the zwitterionic character leads to the formation of a potential well on S_1 (dashed line in Figure 8) due to an avoided crossing between the π^2 and π^{*2} configurations along the torsion. In the absence of a polar solvent the highly polar geometry is unstable and additional motions are needed in the molecule to restore the charge balance (Figure 8). They are realized at the individual CoIn in different ways discussed in section 3.2.3. In case of the nonpolar $CoIn_{Ac}$ and $CoIn_S$ the tilt as third coordinate becomes essential.

3.2.5.3. Seam $CoIn_S$ – $CoIn_{Ac}$. We found that both $CoIn_S$ and $CoIn_{Ac}$ constitute minimum energy structures on a common accessible low lying CoIn seam that is located in the pyramidalization/tilt plane. In the following its topographical features and implications in the photoisomerization are discussed.

In the past couple of years quantum dynamic and semiclassical simulations have shown that nonadiabatic events can occur away from the minimum energy CoIn as long as the nonadiabatic coupling terms remain large.^{86,100–102} Pursuing this idea, research advanced to hyperdimensional curves of CoIn called seams, constituting a continuous manifold of structures accessible from the FC point that allow an efficient decay to a lower lying state. In the more rigorous definition a seam constitutes a minimum energy path (MEP) in the IS connecting CoIn of minimum energy. With the recent developments^{103–106} it has become possible to study their structural and electronic properties.^{107–109} These seams can either run parallel to or cross the ES MEP, in each case having a substantial influence on the reaction mechanism.^{86,109–111} They have become a useful instru-

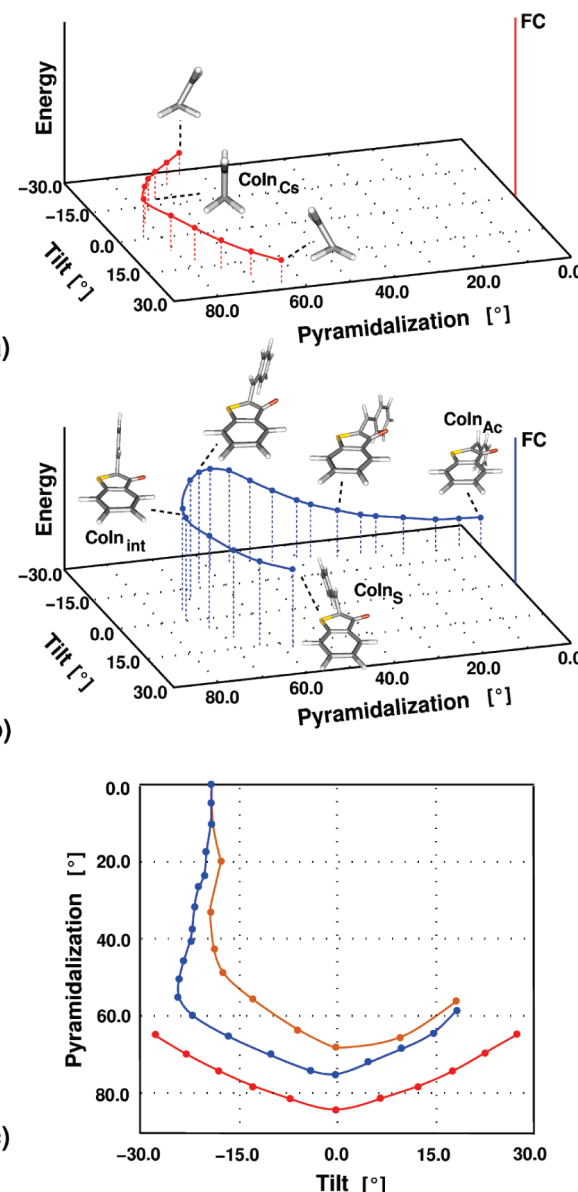


Figure 9. CoIn seam mediating the cis–trans isomerization of ethylene (a) and HTI (b) obtained by the linear interpolation scheme outlined in the Supporting Information. Comparison of the topographies of both seams is carried out in the coordinate space of pyramidalization and tilt. (c) Geometric relation between the ethylene seam (red) and the HTI seam at SA-2-CASSCF(10/9) (blue) and MS-2-CASPT2(14/13) (brown) levels.

ment to elucidate dynamic features of photochemical systems that cannot be explained just by following the ES MEP.

In order to obtain a low lying CoIn seam, the IS was explored using the three-step procedure summarized in section 2.1 and outlined in the Supporting Information. We made use of the fact that HTI should act as a nonpolar ethylene derivative as long as the p_z orbital of the bridging carbon atom C_1 does not interact with the oxygen lone pair. For this constellation the HTI seam topography should closely resemble the seam segment for ethylene presented in Figure 9a.¹¹² The ethylene seam connects two mirror-symmetric tilted/pyramidalized geometries via a TS of C_S symmetry ($CoIn_{Cs}$). The higher symmetry allows its localization using common gradient-based methods. Several conclusions for the topography of the HTI seam can be drawn from the ethylene example: (a) the active coordinates in the IS space are tilt and pyramidalization, while the torsion stays at

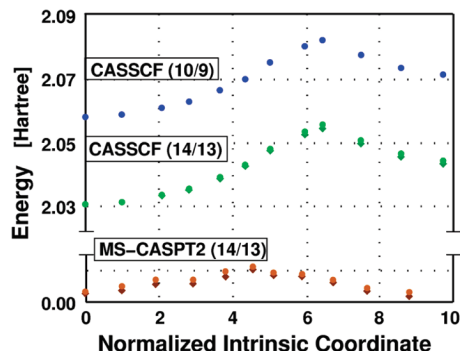


Figure 10. SA-2-CASSCF(10/9), SA-2-CASSCF(14/13), and MS-2-CASPT2(14/13) energies for selected points along the CoIn seam between CoIn_{Ac} and CoIn_S , plotted against the normalized length of the seam in the full Cartesian space. The blue and the green dots follow the CASSCF seam (blue line in Figure 9c); the brown dots follow the CASPT2 corrected seam (brown line in Figure 9c).

90°; (b) a straight linear interpolation between CoIn_{Ac} and CoIn_S will give only a poor starting guess for the subsequent optimization, since a CoIn_{Cs} -like intermediate is required (i.e., tilt and pyramidalization change asynchronously along the seam). According to (b) an intermediate structure, CoIn_{int} , was located in a series of constrained optimizations for a tilt fixed to 0° (see the Supporting Information for details). Characteristic for the intermediate structure is the large pyramidalization angle of 74.9°, similar to the value found for CoIn_{Cs} of 84.2° in ethylene. The new geometry was used as a reference point to determine the tilt angle of all structures along the seam (see Supporting Information for details). The obtained seam is presented in Figure 9b.

As expected, the seam segment above 60° of pyramidalization resembles the seam segment of ethylene (blue vs red line in Figure 9c). This finding is of global importance, since it suggests that nonpolar polyenes or such that exhibit nonpolar features possess similar minimum energy CoIn and comparable seam topography. Deviations from the general trend can be ascribed to individual substituent patterns. The molecular asymmetry of HTI is reflected in the asymmetry of the seam with respect to CoIn_{int} and the shift of TS to a negative tilt angle of -9.9°. In the region of 0°–60° pyramidalization the interaction of the oxygen lone pair with the bridging carbon atom C_1 determines the seam topography.

Perturbation treatment was applied to check the relative energies on the CoIn_S – CoIn_{Ac} seam. On the MS-2-CASPT2 level the dynamic correlation especially needed to describe the zwitterionic state is recovered, leading to dominant zwitterionic contributions in the GS wave function and to a rescaling of the energetic position of GS and ES at the seam. The degeneracy found on the SA-2-CASSCF level is lifted up to maximal 0.5 eV (Table 2). We found that CASSCF overestimates the repulsion of the paired electrons in the zwitterionic state and predicts shorter interatomic distances in the $-(\text{CH})_3-$ kink. Via a scan toward longer interatomic distances in the $-(\text{CH})_3-$ kink, a reduction of the energy gap to less than 0.1 eV was achieved. The result is shown in Figure 9c (brown line) (structures provided in the Supporting Information). In Figure 10 the energetic profile of the seam at different levels of theory is plotted against the normalized length of the seam in the full Cartesian space.¹¹³ The blue and green dots follow the seam optimized at the SA-2-CASSCF(10/9) level; the brown dots follow the MS-2-CASPT2(14/13) corrected seam (including reoptimization). Expanding the active space from (10/9) to (14/13) does not alter the energetic shape of the seam; i.e., it does

not resolve the dynamic correlation inconsistency problem. Only when the perturbative correction is applied, the region of pure $\pi\pi^*$ character (around CoIn_S) is stabilized effectively.

Both CASSCF and CASPT2 predict that the optimized seam can be accessed from the FC point. The incorporation of dynamic correlation effects flattens the PES (Table 2) and the seam, respectively. From the topography of the PES (Figure 7) and of the seam (Figure 9b), we can deduce that the complete region between CoIn_{Ac} and CoIn_S is reachable, allowing an efficient nonradiative decay to the GS. For the decay through CoIn_{Ac} , however, backward pyramidalization is needed after the TS_{SIZ} is passed.

3.2.5.4. Topology of Minimum Energy Points on the CoIn_S – CoIn_{Ac} Seam. Once the CoIn seam is reached, the decay to the GS is possible. Informations about the GS relaxation directions are gained from a first order Taylor expansion in the local branching space (BS)⁷² around the CoIn, spanned by the gradient difference¹¹⁴ and derivative coupling¹¹⁴ vectors. Per construction the BS contains the information about all gradients pointing to possible GS photoproducts.^{115,116} A certain drawback is the fact that the BS is only locally defined and is thus tangential to the true BS, which is curved with respect to the $3N - 6$ coordinate space.^{103,104} Consequently, the Taylor expansion is valid only in the vicinity of a CoIn and is restricted to local information on the emerging pathways. Garavelli et al. proposed a constrained optimization on a hypersphere around a CoIn to correct this inaccuracy,¹¹⁷ whereas an IS analysis introduced recently by Sicilia et al. provides a BS correct to second order.^{103,104} The size of the molecule allows none of these corrections.

The expansion was performed on a circular grid around each CoIn in equidistant intervals.¹¹⁸ The resulting topologies of CoIn_S and CoIn_{Ac} are presented in Figure 11 (the gradient difference and derivative coupling vectors for each CoIn are visualized in Figure S5 in the Supporting Information). Both are tilted, exhibiting only one steep gradient. Optimizations from various initial points around CoIn_S on the GS led exclusively to the Z-HTI. Strong repulsive interactions between the doubly occupied sulfur $3p_z$ orbital and the singly occupied $2p_z$ orbital of the bridging carbon atom C_1 promote the disrotatory¹¹⁹ formation of Z-HTI.

Similar calculations at CoIn_{Ac} show that both E- and Z-HTI can be formed with equal probability. Both gradients stay indistinguishable in the Taylor expansion as the TS line separating both slopes cannot be found within the first order approximation. The major contribution to the GS gradient is the repulsive force between the lone pair of the oxygen and the singly occupied $2p_z$ orbital of the bridging carbon atom C_1 . In conclusion, we expect no preferential formation of either isomer in the region of CoIn_{Ac} . For completeness, we note the possible formation of a metastable byproduct, containing an oxetene ring. The formation of such a cyclic structure has already been observed in the acrolein³¹ photochemistry. The tilted topology of CoIn_{Ac} suggests that its formation is unlikely.

An important conclusion from the seam analysis between CoIn_S and CoIn_{Ac} is that at no point can an exclusive decay to E-HTI be observed. CoIn_S allows only back reaction to the Z isomer; CoIn_{Ac} favors both pathways to Z and E isomers equally. Along the connecting seam, starting from CoIn_S , we assume that the second pathway opens gradually. This feature agrees with the measured product quantum yield for the $Z \rightarrow E$ photoreaction of less than 50%.

3.2.5.5. E → Z PES. The ES PES relevant for the E → Z isomerization is plotted in Figure 12 between 180° and 90°

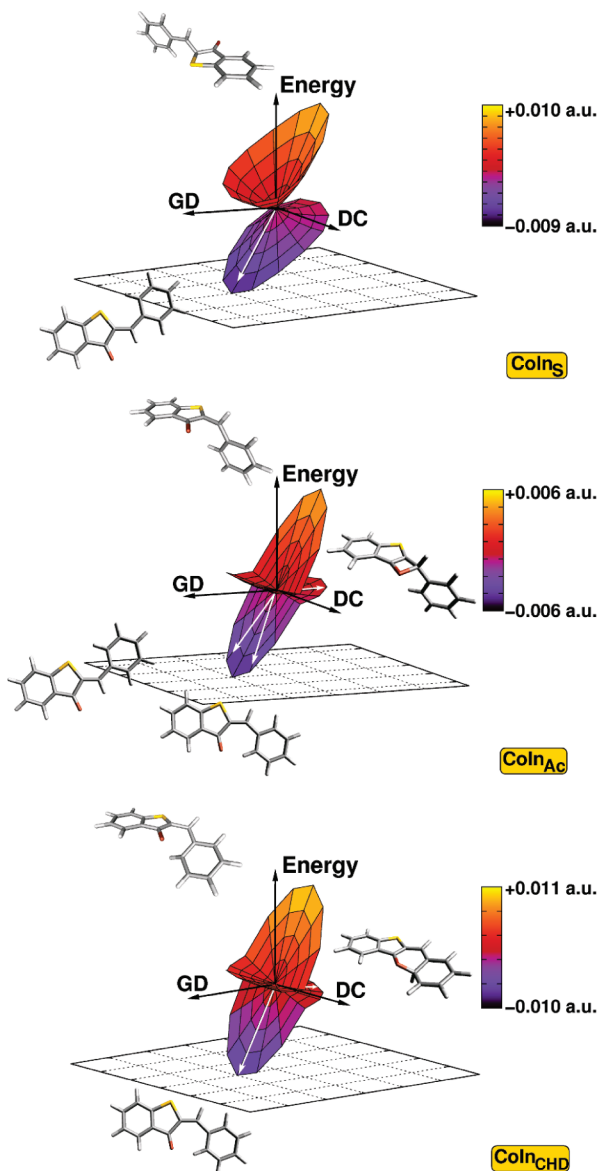


Figure 11. Topologies of CoIn_S , CoIn_Ac , and CoIn_CHD with the corresponding GS products.

torsion and between -30° and 30° pyramidalization. The range of the pyramidalization coordinate is now adapted to the isomerization activity from the E-side. The region between 90° and 120° torsion is scaled according to the MS-2-CASPT2 corrected energy for CoIn_Ac (see section 1.2 in the Supporting Information). Per construction the torsion runs counterclockwise (Figure 6a). Depending on the initial starting point for the relaxed 2D scan, the optimized PES acquires very different topographical features.

Sampling the ES from the planar $\text{Min}_{\text{S}1\text{E}}$ yields a shallow surface (upper surface in Figure 12) for 140° – 180° torsion, similar to the one obtained for the Z → E isomerization in the region between 0° and 40° . When CoIn_CHD is taken as starting point, a broad valley (lower surface in Figure 12), defining a wide S_1/S_0 near-degeneracy region, characterizes the 2D S_1 surface. The existence of multiple solutions to a constrained optimization problem implies that further coordinates are necessary for the unique construction of the E → Z relaxation surface. Shear-like deformations of the phenyl ring toward the oxygen decreasing the C_2 – C_1 – C_3 angle mediate the transition from the upper to the lower surface.

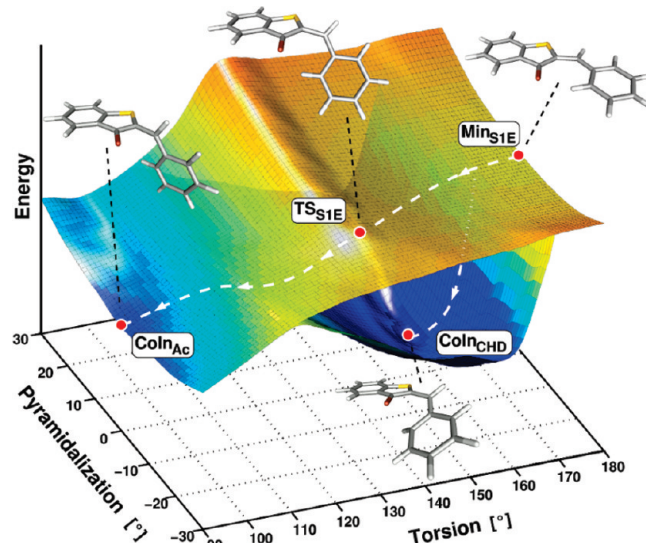


Figure 12. S_1 PES for the E → Z reaction from a relaxed 2D scan in the region of 90° – 180° torsion and of -30° to 30° pyramidalization. Two stable surfaces arise for different residual deformations. The upper surface is optimized starting at the FC point. The lower surface is obtained utilizing CoIn_CHD as an initial point. Both surfaces coincide in the regions of 90° – 110° and 170° – 180° torsion. Approximate ES reaction pathways are derived from the topography of both PES (dashed white lines).

First we describe the specifics of the upper PES. From the FC^* region we observe an initial negative pyramidalization toward CoIn_S^* . The analogous motion on the Z-side was a positive pyramidalization toward CoIn_S . Both types of pyramidalization are associated with a disrotatory rotation in accordance with the Woodward–Hoffmann rules (the reader is referred to the Supporting Information for a valence bond (VB) aided discussion). Conrotatory motions are energetically hindered, blocking CoIn_S for the E-side and CoIn_S^* from the Z-side. From the previous discussion we know that CoIn_S leads to the Z isomer. Consequentially, we can deduce that CoIn_S^* leads to the E isomer and photostabilizes the system. However, due to the unfavorable alignment of hemithioindigo and hemistilbene (Figure 5d), CoIn_S^* is destabilized notably and its formation is possible, but unlikely. For this reason we restricted the 2D scan to the interval between -30° and 30° pyramidalization, focusing on the dominant relaxation pathway toward CoIn_Ac (upper white dashed line in Figure 12). The latter acts as a branching point toward both isomers.

We now turn to the characterization of the lower PES. Already at 10° torsion the E-HTI can relax down to the region around CoIn_CHD . A broad area of near degeneracy is found that photostabilizes the E isomer. This statement is supported by a Taylor expansion in the BS around CoIn_CHD (Figure 11) yielding one pronounced gradient toward E-HTI. The possible formation of a polycyclic chromene derivative introduces a side reaction, similar to the light induced ring closure in cis-diarylethenes.^{72,94,95} The formed closed-ring product is metastable and relaxes rapidly to E-HTI.

The presence of a broad S_0/S_1 near-degeneracy region around CoIn_CHD suggests the existence of a low lying CoIn seam connecting CoIn_CHD to CoIn_Ac . Constrained optimizations based on a prior linear interpolation between both CoIn were not successful. We ascribe this to the increasing contributions from the $n\pi^*$ configuration to the ES wave function along the seam that influences the direction of the ES gradient. A recent study¹⁰⁸ of the cis–trans isomerization of O-hydroxybenzaldehyde

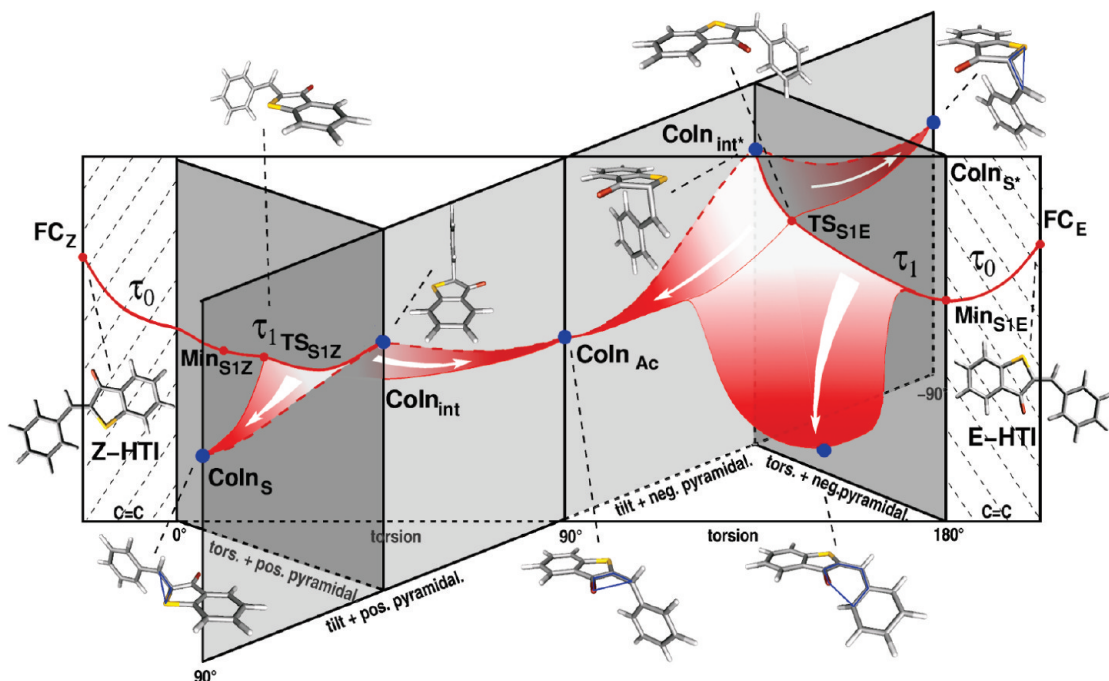


Figure 13. Schematic representation of the reaction pathways on the ES PES. The out-of-plane torsion is symbolized by a transparent plane connecting Z and E. The shaded planes sketch the effect of bond length rearrangements in the planar geometries. The diagonal light-gray plane combines pyramidalization and tilt for a constant torsional angle of 90° and contains a 1D projection of the CoIn seam connecting CoIn_S and CoIn_{S*} via CoIn_{Ac} (red dashed line). Both dark-gray surfaces connecting the torsional plane and the CoIn_S/CoIn_{S*} seam plane symbolize modes of contrarotatory pyramidalization and torsion.

showed that, depending on the deformations along the seam, the S₁ wave function can be dominated either by the zwitterionic or by the nπ* configuration. Thus, an optimization with a more elaborate method such as MS-CASPT2 is needed to locate the seam, but is still out of reach.

To summarize, E-HTI is expected to experience high losses via a fast photostable pathway through CoIn_{CHD}. Consequently, the quantum yield for the E → Z isomerization should be smaller compared to the Z → E process.

4. Connecting Theory and Experiment

The results provided from experiment and theory demonstrate that the cis–trans isomerization of HTI conceals a complex reaction mechanism, offering several decay channels through an extended, low lying, accessible CoIn seam. As a schematic representation, Figure 13 shows the energetic profile of the ES reaction pathways. The out-of-plane torsion as the main reaction coordinate is displayed in the transparent plane connecting Z and E. The most left and right segments of that plane visualize the effect from bond length rearrangements in the planar structures. The elongation of the central carbon–carbon bond was found to give the major initial energetic stabilization. The diagonal light-gray plane, crossing the torsional plane at 90°, combines pyramidalization and tilt for a constant torsional angle of 90°¹²⁰ and contains a 1D projection of the CoIn seam connecting CoIn_S and CoIn_{S*} via CoIn_{Ac} (red dashed line). Based on the arguments derived for the optimized seam segment CoIn_S/CoIn_{Ac} (positive pyramidalization, see Figure 9b), we can readily extrapolate the seam to the region of CoIn_{S*} (negative pyramidalization). We expect this extension to be shifted to higher energy due to the unfavorable orientation of the fragments. In support of our speculations we searched for the intermediate structure CoIn_{int*} on the seam segment CoIn_{Ac}/CoIn_{S*}, which is the analogue to CoIn_{int}. The optimized geometry was found to lie energetically above the E-HTI FC point.

Evolution from the FC regions of Z- and E-HTI is driven by disrotatory modes accompanied by pyramidalization and torsion of opposite signs (see scheme S1 in the Supporting Information). This is indicated by the two dark-gray surfaces connecting the torsional plane to the seam plane.

4.1. The Z → E Reaction. After excitation of the Z isomer the initial S₁ relaxation is dominated by rapid bond length rearrangement, mainly of the central C=C double bond, accompanied by solvent adjustment to the altered electron density distribution. Both processes contribute to the experimental signal. The reaction then proceeds in a flat region of the ES where gradual redistribution of the energy into torsion and pyramidalization drives the molecule into the local minimum Min_{S1Z}. Evidence for the existence of such a local minimum is provided by the detected weak fluorescence. As the ππ* and the dark nπ* states (section 3.2.1) in the FC region are nearly of the same energy, we assume the opening of an additional relaxation pathway via a singlet (nπ*)–triplet (ππ*)–singlet (π²) cascade. Both pathways contribute to the reaction rate $k_0 = 1/\tau_0$ with $\tau_0 = 2.0 \pm 0.8$ ps, observed experimentally. From the absorption changes in the range of the GS band at 425 nm, we deduce that the yield ϕ_{isc} of triplet formation is similar to the yield of isomerization $\phi_{\text{pc},Z}$; i.e., $\phi_{\text{isc}} \approx 23\%$. This value is deduced from the observation that the amplitude of the bleach recovery and the final offset spectrum at 435 nm (representing the photochemical conversion Z to E) are similar. Consequently, approximately 77% of the molecules proceed along the singlet pathway.

The second time constant $\tau_1 = 10 \pm 1$ ps is attributed to the overcoming of the shallow ES barrier and the decay into the GS at the CoIn seam. Up to now time-resolved spectroscopy has been unable to characterize the dynamics in the vicinity of the seam, and for the interpretation we rely on our quantum chemical data. We identified two main relaxation channels contributing to the overall rate $k_1 = 1/\tau_1$: a reactive channel

mediated by CoIn_{Ac} with a predicted educt/product distribution of 1/1 (i.e., 23%/23%) and a photostabilizing channel via CoIn_S with 31% contribution ($77\% - 23\% - 23\% = 31\%$). Based on these considerations the efficient reactive rate $k_{\text{eff},Z \rightarrow E}$ leading from Min_{S1Z} to the E isomer can be estimated to be $k_{\text{eff},Z \rightarrow E} = 1/(16.8 \pm 1.6) \text{ ps}^{-1}$ (see Figure S6 in the Supporting Information). At no point along the accessible part of the CoIn_S – CoIn_{Ac} seam is an exclusive decay to *E*-HTI observed.

4.2. The $E \rightarrow Z$ Reaction. The initial relaxation process from the FC point of *E*-HTI (FC_E) is comparable to the one on the Z-side and leads to the planar minimum Min_{S1E} . There are no experimental indications of possible triplet contributions, and we assume that 100% of the molecules proceed via the singlet relaxation pathway. During the first several hundred femtoseconds ($\tau_0 = 260 \pm 80 \text{ fs}$) only bond relaxation takes place. Two pathways emerge from Min_{S1E} . One proceeds primarily along the torsion coordinate toward CoIn_{Ac} ; a second one, involving the shear-like deformations of hemistilbene toward the oxygen, opens the valley to CoIn_{CHD} . The first pathway is the photoreactive pathway and is mechanistically comparable to the one discussed for the $Z \rightarrow E$ isomerization. Taking again the predicted 1/1 educt/product distribution at CoIn_{Ac} and the low quantum yield of $\phi_{\text{pc},E} \approx 5.3\%$ as a basis, we estimate that only 10.6% of all molecules follow this path. The remaining 89.4% evolve along the second pathway, the rapid nonreactive deactivation via CoIn_{CHD} . The effective reaction rate $k_{\text{eff},E \rightarrow Z}$ for Z -HTI formation from Min_{S1E} can also be determined from the experimental data. With the specific values for τ_1 and $\phi_{\text{pc},E}$ we estimate $k_{\text{eff},E \rightarrow Z} = 1/(11.3 \pm 3.7) \text{ ps}^{-1}$, a value which is close to the one obtained for the reactive branch of the $Z \rightarrow E$ reaction and is much slower than the direct nonreactive decay rate $k_{\text{NR}} \approx 1/(1.3 \pm 0.4) \text{ ps}^{-1}$ via CoIn_{CHD} . The observed high rate of the nonreactive decay is explained well by the calculations where the 2D scan reveals that *E*-HTI can relax into the CoIn_{CHD} valley already at 10° torsion. The substantial differences observed for the $Z \rightarrow E$ and $E \rightarrow Z$ reactions for time constants and quantum yields can be explained by the existence of an efficient photostabilizing channel accessible only from *E*-HTI and not by differences in the isomerization mechanism itself.

5. Conclusions

Photoisomerization of a minimal model including heteroatoms was investigated experimentally and theoretically. As example, we selected the Z/E isomerization of photochromic HTI in an nonpolar solvent.

The reaction was followed in real time using UV-vis pump–probe experiments, which revealed ultrafast processes for both directions. Considerable differences in time constants and quantum yield were observed. High-level quantum chemical calculations were performed to correlate the relevant time steps with the atomistic mechanisms and to identify the driving forces on the reaction pathways.

We found that the weakly heterosymmetric biradicaloid character of HTI determines the driving force for the isomerization in both directions. Charge separation and charge balance recovery on the reaction pathway are mediated by the electron-donating or -withdrawing character of the heteroatoms and define the structure, energetic position, and accessibility of a number of CoIn. In general, every Z/E isomerization has to pass through a geometry where both interacting fragments are electronically decoupled. Electrostatic forces prevent excessive charge separation associated with this decoupling and are realized at the CoIn.

Using VB and MO theory we characterized the relevant CoIn seam and demonstrated the significance of heteroatoms. Their

inclusion opens a whole new range of possibilities to stabilize the reaction pathway by adjustment of the electrostatic interactions. On one hand, this new diversity comes at the expense of additional loss channels. In the presented minimal model such a loss channel with a strongly heterosymmetric biradicaloid character opens on the E-side and acts as a very efficient trap. On the other hand, the new diversity allows for fast photochemical switching, even in bulky systems such as HTI. Slow skeletal deformations are replaced by fast charge redistributions using substituent effects in heterocycles.

Acknowledgment. We thank Karola Rück-Braun and Torsten Schadendorf for providing the studied HTI compound. Financial support by DFG through SFB749 and the excellence cluster Munich Center for Advanced Photonics (MAP) is gratefully acknowledged.

Supporting Information Available: Details on the derivation of the reactive coordinates (torsion, pyramidalization, tilt) and the construction of the relaxed PES; introduction of the “linear interpolation approach” used for obtaining the CoIn seam; VB-aided discussion of the Woodward–Hoffmann “allowed” disrotatory rotation upon isomerization and the consequences for the reaction mechanism; visualization of the delocalized (π, π^*) and localized (A,B) basis using the example of CoIn_{Ac} and CoIn_{CHD} ; HOMO and LUMO orbitals of all stationary CoIn in the localized basis; visualization of the gradient difference and derivative coupling vectors used for the construction of the Taylor expansion around CoIn_S , CoIn_{Ac} , and CoIn_{CHD} ; Cartesian coordinates for the structures discussed in the paper (minima, transition states, minimum energy CoIn, CASSCF seam, CASPT2 corrected seam); complete references for Gaussian 03, revision D.01, Molpro 2006.1, and Molcas, revision 7.4. This material is available free of charge via the Internet at <http://pubs.acs.org>.

References and Notes

- (1) Baum, P.; Yang, D. S.; Zewail, A. H. *Science* **2007**, *318* (5851), 788–792.
- (2) Steinle, W.; Rück-Braun, K. *Org. Lett.* **2003**, *5*, 141–144.
- (3) Lougheed, T.; Borisenko, V.; Hennig, T.; Rück-Braun, K.; Woolley, G. A. *Org. Biomol. Chem.* **2004**, *2*, 2798–2801.
- (4) Herre, S.; Steinle, W.; Rück-Braun, K. *Synthesis* **2005**, *3297*, 3300.
- (5) Schadendorf, T.; Hoppmann, C.; Rueck-Braun, K. *Tetrahedron Lett.* **2007**, *48*, 9044–9047.
- (6) Cordes, T. Dissertation, LMU Munich, 2008.
- (7) Cordes, T.; Weinrich, D.; Kemps, S.; Reisselmann, K.; Herre, S.; Hoppmann, C.; Rück-Braun, K.; Zinth, W. *Chem. Phys. Lett.* **2006**, *428* (1–3), 167–173.
- (8) Cordes, T.; Elsner, C.; Herzog, T. T.; Hoppmann, C.; Schadendorf, T.; Summerer, W.; Rück-Braun, K.; Zinth, W. *Chem. Phys.* **2009**, *358*, 103–110.
- (9) Cordes, T.; Heinz, B.; Regner, N.; Hoppmann, C.; Schrader, T. E.; Summerer, W.; Rück-Braun, K.; Zinth, W. *ChemPhysChem* **2007**, *8* (11), 1713–1721.
- (10) Cordes, T.; Schadendorf, T.; Rück-Braun, K.; Zinth, W. *Chem. Phys. Lett.* **2008**, *455*, 197–201.
- (11) Cordes, T.; Schadendorf, T.; Priewisch, B.; Rück-Braun, K.; Zinth, W. *J. Phys. Chem. A* **2008**, *112* (4), 581–588.
- (12) Plötner, J.; Dreuw, A. J. *J. Phys. Chem. A* **2009**, *113* (43), 11882.
- (13) Bearpark, M. J.; Bernardi, F.; Clifford, S.; Olivucci, M.; Robb, M. A.; Vreven, T. *J. Phys. Chem. A* **1997**, *101*, 3841.
- (14) Quenneville, J.; Martínez, T. J. *J. Phys. Chem. A* **2003**, *107*, 829.
- (15) Barbatti, M.; Ruckenbauer, M.; Szymczak, J. J.; Aquino, A. J. A.; Lischka, H. *Phys. Chem. Chem. Phys.* **2008**, *10*, 482.
- (16) Bonacić-Koutecký, V.; Michl, J.; Köhler, J. *Chem. Phys. Lett.* **1984**, *1*, 440.
- (17) Bearpark, M. J.; Olivucci, M.; Wilsey, S.; Bernardi, F.; Robb, M. A. *J. Am. Chem. Soc.* **1995**, *117*, 6944.
- (18) Ben-Nun, M.; Martínez, T. J. *Chem. Phys.* **2000**, *259*, 237.
- (19) Barbatti, M.; Paier, J.; Lischka, H. *J. Chem. Phys.* **2004**, *121* (23), 11614.

- (20) Garavelli, M. *Theor. Chem. Acc.* **2006**, *116*, 87.
- (21) Ruiz, D. S.; Cembran, A.; Garavelli, M.; Olivucci, M.; Fuss, W. *Photochem. Photobiol.* **2002**, *76*, 622.
- (22) Szymczak, J. J.; Barbatti, M.; Lischka, H. *J. Phys. Chem. A* **2009**, *113* (43), 11907.
- (23) Michl, J.; Bonačić-Koutecký, V. In *Electronic Aspects of Organic Photochemistry*; VCH: New York, 1990.
- (24) Gonzalez-Luque, R.; Garavelli, M.; Bernardi, F.; Merchan, M.; Robb, M. A.; Olivucci, M. *Proc. Natl. Acad. Sci. U.S.A.* **2000**, *97*, 9379.
- (25) Tomasello, G.; Olaso-Gonzalez, G.; Altoe, P.; Stenta, M.; Serrano-Andres, L.; Merchan, M.; Orlandi, G.; Bottoni, A.; Garavelli, M. *J. Am. Chem. Soc.* **2009**, *131*, 5172.
- (26) Rajput, J.; Rahbek, D. B.; Andersen, L. H.; Hirshfeld, A.; Sheves, M.; Altoe, P.; Orlandi, G.; Garavelli, M. *Angew. Chem., Int. Ed.* **2010**, *49*, 1790.
- (27) Frutos, L. M.; Andruniow, T.; Santro, F.; Ferre, N.; Olivucci, M. *Proc. Natl. Acad. Sci. U.S.A.* **2007**, *104* (19), 7764.
- (28) Groenhof, G.; Bouxin-Cademartory, M.; Hess, B.; de Visser, S. P.; Berensen, H. J. C.; Olivucci, M.; Mark, A. E.; Robb, M. A. *J. Am. Chem. Soc.* **2004**, *126*, 4228.
- (29) Groenhof, G.; Schäfer, L. V.; Boggio-Pasqua, M.; Grubmüller, H.; Robb, M. A. *J. Am. Chem. Soc.* **2008**, *130*, 3250.
- (30) Boggio-Pasqua, M.; Robb, M.; Groenhof, G. *J. Am. Chem. Soc.* **2009**, *131*, 13580.
- (31) Reguero, M.; Olivucci, M.; Bernardi, F.; Robb, M. A. *J. Am. Chem. Soc.* **1994**, *116*, 2103.
- (32) Wilsey, S.; Bearpark, M. J.; Bernardi, F.; Olivucci, M.; Robb, M. A. *J. Am. Chem. Soc.* **1996**, *118*, 176.
- (33) Barbatti, M.; Aquino, A. J. A.; Lischka, H. *J. Phys. Chem. A* **2005**, *109* (23), 5168.
- (34) Wadsworth, D. H.; Detty, M. R. *J. Org. Chem.* **1980**, *45*, 4611–4615.
- (35) Guha, S. K.; Mitra, A. K.; Gandhi, R. S. *J. Indian Chem. Soc.* **1968**, *45*, 997–1001.
- (36) Guha, S. K.; Chatterjea, J. N.; Mitra, A. K. *Chem. Ber.* **1961**, *94*, 3297–3303.
- (37) Cordes, T.; Regner, N.; Heinz, B.; Borysova, E.; Ryseck, G.; Gilch, P. *J. Photochem. Photobiol. A: Chem.* **2009**, *206*, 10–17.
- (38) Wilhelm, T.; Piel, J.; Riedle, E. *Opt. Lett.* **1997**, *22*, 1494–1496.
- (39) Riedle, E.; Beutter, M.; Lochbrunner, S.; Piel, J.; Schenkl, S.; Sporlein, S.; Zinth, W. *Appl. Phys. B: Lasers Opt.* **2000**, *71*, 457–465.
- (40) Huber, R.; Satzger, H.; Zinth, W.; Wachtveitl, J. *Opt. Commun.* **2001**, *194*, 443–448.
- (41) Seel, M.; Wildermuth, E.; Zinth, W. *Meas. Sci. Technol.* **1997**, *8*, 449–452.
- (42) Satzger, H.; Zinth, W. *Chem. Phys.* **2003**, *295* (3), 287–295.
- (43) Werner, H. J.; et al. *Molpro*, version 2006.1; Cardiff, U.K.
- (44) Anderson, K.; et al. *Molcas*, revision 7.4; Department of Theoretical Chemistry, Chemistry Center, University of Lund: Lund, Sweden, 2000.
- (45) Frisch, M. J.; et al. *Gaussian 03*, revision D.01; Gaussian Inc.: Wallingford, CT2004.
- (46) Roos, B. O. In *Advanced Chemistry and Physics: Ab Initio Methods in Quantum Chemistry II*; Wiley: Chichester, U.K., 1987; p 399.
- (47) Andersson, K.; Malmqvist, P.-Å.; Roos, B. O.; Sadlej, A. J.; Wolinski, K. *J. Chem. Phys.* **1990**, *94*, 5483.
- (48) Andersson, K.; Malmqvist, P.-Å.; Roos, B. O. *J. Chem. Phys.* **1992**, *96*, 1218.
- (49) Finley, J.; Malmqvist, P.-Å.; Roos, B. O.; Serrano-Andrés, L. *Chem. Phys. Lett.* **1998**, *288*, 299.
- (50) Malmqvist, P.-Å.; Roos, B. O. *Chem. Phys. Lett.* **1989**, *155*, 189.
- (51) Bader, R. F. W.; Carroll, M. T.; Cheeseman, J. R.; Chang, C. *J. Am. Chem. Soc.* **1987**, *109*, 7968.
- (52) Lorentzon, J.; Malmqvist, P.-Å.; Fülscher, M.; Roos, B. *Theor. Chem. Acc.* **1995**, *91*, 91.
- (53) Asturiol, D.; Lasorne, B.; Worth, G. A.; Robb, M. A.; Blancafort, L. *Phys. Chem. Chem. Phys.* **2010**, *12*, 4949.
- (54) Merchan, M.; Serrano-Andrés, L. *J. Am. Chem. Soc.* **2003**, *125*, 8108.
- (55) Ghigo, G.; Roos, B. O.; Malmqvist, P.-Å. *Chem. Phys. Lett.* **2004**, *396*, 142.
- (56) Roos, B. O.; Andersson, K. *Chem. Phys. Lett.* **1995**, *245*, 215.
- (57) Roos, B. O.; Andersson, K.; Fülscher, M. P.; Serrano-Andrés, L.; Pierloot, K.; Merchán, M.; Molina, V. *J. Mol. Struct. (THEOCHEM)* **1996**, *388*, 257.
- (58) Ditchfield, R.; Hehre, W. J.; Pople, J. A. *J. Chem. Phys.* **1971**, *54*, 724.
- (59) Franci, M. M.; Pietro, W. J.; Hehre, W. J.; Binkley, J. S.; DeFrees, D. J.; Pople, J. A.; Gordon, M. S. *J. Chem. Phys.* **1982**, *77*, 3654.
- (60) Rassolov, V. A.; Ratner, M. A.; Pople, J. A.; Redfern, P. C.; Curtiss, L. A. *J. Comput. Chem.* **2001**, *22*, 976.
- (61) Ragazos, I. N.; Robb, M. A.; Bernardi, F.; Olivucci, M. *Chem. Phys. Lett.* **1992**, *197*, 217.
- (62) Bearpark, M. J.; Robb, M. A.; Schlegel, H. B. *Chem. Phys. Lett.* **1994**, *223*, 269.
- (63) Cordes, T.; Schadendorf, M.; Lipp, M.; Rück-Braun, K.; Zinth, W. *Ultrafast Phenomena XVI*; Springer-Verlag: Berlin, 2009; pp 319–321.
- (64) Strickler, S. J.; Berg, R. A. *J. Chem. Phys.* **1962**, *37*, 814.
- (65) Becke, A. D. *J. Chem. Phys.* **1993**, *98*, 5648.
- (66) Lee, C.; Yang, W.; Parr, R. G. *Phys. Rev. B* **1988**, *37*, 785.
- (67) Stephens, P. J.; Devlin, F. J.; Chabalowski, C. F.; Frisch, M. J. *J. Phys. Chem.* **1994**, *98*, 11623.
- (68) Asturiol, D.; Lasorne, B.; Robb, M. A.; Blancafort, L. *J. Phys. Chem. A* **2009**, *113* (38), 10211.
- (69) van der Lugt, W. T. A. M.; Oosterhoff, L. *J. Chem. Commun.* **1968**, 1235.
- (70) van der Lugt, W. T. A. M.; Oosterhoff, L. *J. J. Am. Chem. Soc.* **1969**, *91*, 6042.
- (71) Klessinger, M.; Michl, J. In *Excited States and Photochemistry of Organic Molecules*; VCH: New York, 1995.
- (72) Atchity, G. J.; Xantheas, S. S.; Ruedenberg, K. *J. Chem. Phys.* **1991**, *95*, 1862.
- (73) Celani, P.; Ottani, S.; Olivucci, M.; Bernardi, F.; Robb, M. A. *J. Am. Chem. Soc.* **1994**, *116*, 10141.
- (74) Palmer, I.; Ragazos, I.; Robb, I. *J. Am. Chem. Soc.* **1993**, *115*, 673.
- (75) Olivucci, M.; Bernardi, M.; Celani, P.; Ragazos, I. N.; Robb, M. A. *J. Am. Chem. Soc.* **1994**, *116*, 1077.
- (76) Bernardi, F.; Olivucci, M.; McDouall, J. J. W.; Robb, M. A. *J. Chem. Phys.* **1988**, *89*, 6365.
- (77) Olivucci, M.; Robb, M. A.; Bernardi, F. In *Conformational Analysis of Molecules in Excited States*; Wiley VCH: New York, 2000; pp 297–366.
- (78) Michl, J.; Bonačić-Koutecký, V. *Tetrahedron* **1988**, *44*, 7559.
- (79) Liu, R. S. H.; Hammond, G. S. *Proc. Natl. Acad. Sci. U.S.A.* **2000**, *97*, 11153.
- (80) Liu, R. S. H. *Acc. Chem. Res.* **2001**, *34*, 555.
- (81) Liu, R. S. H.; Hammond, G. S. *Chem. Eur.* **2001**, *7*, 4536.
- (82) Fuss, W.; Kosmidis, C.; Schmid, W. E.; Trushin, S. A. *Angew. Chem., Int. Ed.* **2004**, *43*, 4178.
- (83) Celani, P.; Bernardi, F.; Olivucci, M.; Robb, M. A. *J. Chem. Phys.* **1995**, *102*, 5733.
- (84) Garavelli, M.; Celani, P.; Bernardi, F.; Robb, M. A.; Olivucci, M. *J. Am. Chem. Soc.* **1997**, *119*, 11487.
- (85) Celani, P.; Garavelli, M.; Ottani, S.; Bernardi, F.; Robb, M. A.; Olivucci, M. *J. Am. Chem. Soc.* **1995**, *117*, 11584.
- (86) Boggio-Pasqua, M.; Ravaglia, M.; Bearpark, M. J.; Garavelli, M.; Robb, M. A. *J. Phys. Chem. A* **2003**, *107*, 11139.
- (87) Kosma, K.; Trushin, S. A.; Fuss, W.; Schmid, W. E. *J. Phys. Chem. A* **2008**, *112* (33), 7514.
- (88) Turro, N. J. In *Modern Molecular Photochemistry*; Benjamin-Cummings: Menlo Park, CA, 1991.
- (89) Gilbert, A.; Baggot, J. In *Essentials of Molecular Photochemistry*; Blackwell Science: Oxford, 1991.
- (90) Garavelli, M.; Celani, P.; Bernardi, F.; Robb, M. A.; Olivucci, M. *J. Am. Chem. Soc.* **1997**, *119*, 6891.
- (91) Garavelli, M.; Bernardi, F.; Celani, P.; Robb, M. A.; Olivucci, M. *J. Photochem. Photobiol. A: Chem.* **1998**, *114*, 109.
- (92) Cordes, T.; Malkmus, S.; Di Girolamo, J.; Lees, W. J.; Nenov, A.; de Vivie-Riedle, R.; Braun, M.; Zinth, W. *J. Phys. Chem. A* **2008**, *112*, 13364.
- (93) Tomasello, G.; Bearpark, M. J.; Robb, M. A.; Orlandi, G.; Garavelli, M. *Angew. Chem., Int. Ed.* **2010**, *49*, 2913.
- (94) Coe, J. D.; Levine, B. G.; Martínez, T. J. *J. Phys. Chem. A* **2007**, *111*, 11302.
- (95) Sobolewski, A.; Domcke, W. *Phys. Chem. Chem. Phys.* **2006**, *8*, 3410.
- (96) Celani, P.; Bernardi, F.; Olivucci, M.; Robb, M. A. *J. Am. Chem. Soc.* **1997**, *119* (44), 10815.
- (97) For stability reasons the different CoIn have been optimized with slightly different active spaces, so the provided comparison on the basis of the relative energies in Table 2 should be considered as only qualitative.
- (98) For each one of the Z and E isomers two equivalent torsional motions can be defined: a clockwise and a counterclockwise.
- (99) The reader is referred to the Supporting Information for a detailed discussion of their construction.
- (100) Geppert, D.; Seyfarth, L.; de Vivie-Riedle, R. *Appl. Phys. B: Laser Opt.* **2004**, *79*, 987.
- (101) Kurtz, L.; Hofmann, A.; de Vivie-Riedle, R. *J. Chem. Phys.* **2001**, *114*, 6151.
- (102) Hofmann, A.; de Vivie-Riedle, R. *Chem. Phys. Lett.* **2001**, *346*, 299.
- (103) Paterson, M. J.; Bearpark, M. J.; Robb, M. A.; Blancafort, L. *J. Chem. Phys.* **2004**, *121*, 11562.
- (104) Sicilia, F.; Blancafort, L.; Bearpark, M. J.; Robb, M. A. *J. Phys. Chem. A* **2007**, *111*, 2182.

- (105) Sicilia, F.; Blancafort, L.; Bearpark, M. J.; Robb, M. A. *J. Chem. Theory Comput.* **2008**, *4*, 257.
- (106) De Vico, L.; Lindh, R. *J. Chem. Theory Comput.* **2009**, *5*, 186.
- (107) Sicilia, F.; Bearpark, M. J.; Blancafort, L.; Robb, M. A. *Theor. Chem. Acc.* **2007**, *118*, 241.
- (108) Migani, A.; Blancafort, L.; Robb, M.; DeBellis, A. *J. Am. Chem. Soc.* **2008**, *130*, 6932.
- (109) Nenov, A.; Kölle, P.; Robb, M. A.; de Vivie-Riedle, R. *J. Org. Chem.* **2010**, *75*, 123.
- (110) Paterson, M. J.; Robb, M. J.; Blancafort, L.; DeBellis, A. D. *J. Phys. Chem. A* **2005**, *109* (33), 7527.
- (111) Altoe, P.; Haraszkiewicz, N.; Gatti, F. C.; Wiering, P. G.; Frochot, C.; Brouwer, A. M.; Balkowski, G.; Shaw, D.; Woutersen, S.; Buma, W. J.; Zerbetto, F.; Orlando, G.; Leigh, D. A.; Garavelli, M. *J. Am. Chem. Soc.* **2009**, *131*, 104.
- (112) The complete CoIn seam for ethylene is more complex and branched;¹⁸ however, the segment shown in Figure 9a is sufficient for the present discussion.
- (113) The intrinsic coordinate is constructed by summing the distances between each pair of successive points on the seam after normalization with respect to the distance between the first pair.
- (114) Domcke, W.; Yarkony, D.; Köppel, H. In *Advanced Series in Physical Chemistry*; World Scientific Publishing: River Edge, NJ, 2004.
- (115) Sellner, B.; Barbatti, M.; Lischka, H. *J. Chem. Phys.* **2009**, *131*, 024312.
- (116) Frutos, L. M.; Sancho, U.; Garavelli, M.; Olivucci, M.; Castaño, O. *J. Phys. Chem. A* **2007**, *111* (15), 2830.
- (117) Garavelli, M.; Celani, P.; Fato, M.; Bearpark, M. J.; Smith, B. R.; Olivucci, M.; Robb, M. A. *J. Phys. Chem. A* **1997**, *101*, 2023.
- (118) Frutos, L. M.; Markmann, A.; Sobolewski, A. L.; Domcke, W. *J. Phys. Chem. B* **2007**, *111* (22), 6110.
- (119) The reader is referred to the Supporting Information for a VB discussion of the reaction mechanism elucidating why the disrotatory motion is preferred.
- (120) The tilt/pyramidalization plane lies orthogonal to the torsional plane. To allow a comprehensible visualization, both planes were drawn under an angle of 45°.

JP107899G